UNIVERSIDADE Ð COIMBRA

Ana Rita dos Santos Bernardo

OPTICAL COHERENCE ELASTOGRAPHY IN DERMATOLOGY

Dissertação no âmbito do Mestrado em Engenharia Biomédica com especialização em Instrumentação Biomédica orientada pelo Professor Doutor José Paulo Pires Domingues e pela Doutora Ana Batista e apresentada ao Departamento de Física da Faculdade de Ciências e Tecnologia da Universidade de Coimbra.

Setembro de 2022

UNIVERSIDADE DE COIMBRA

MESTRADO EM ENGENHARIA BIOMÉDICA

Optical Coherence Elastography in Dermatology

Ana Rita dos Santos Bernardo

Dissertação apresentada à Faculdade de Ciências e Tecnologia da Universidade de Coimbra para cumprimento dos requisitos necessários à obtenção do grau de Mestre em Engenharia Biomédica

Orientadores:

Professor Doutor José Paulo Domingues.

Doutora Ana Batista

1 2 9 0

UNIVERSIDADE Ð
COIMBRA

Coimbra, Setembro 2022

Contents

Agradecimentos

Em primeiro lugar gostaria de agradecer aos meus orientadores professor José Paulo Domingues e Doutora Ana Batista pela oportunidade de trabalhar neste projeto e pela orientação no desenvolvimento e escrita desta dissertação.

À doutora Ana Batista por toda a ajuda, informações, partilha de conhecimento e gentileza no decorrer de todo o trabalho laboratorial. Aos meus colegas de laboratório, João e Inês, por serem sempre prestáveis. A todos os voluntários que se mostram sempre prontos a colaborar e cuja contribuição foi essencial para o desenvolvimento deste trabalho.

A todos que desde o meu primeiro dia em Coimbra me fizeram sentir em casa. Ao João Albuquerque que me mostrou que o DF é uma casa e que todos juntos formamos uma família, que esteve comigo desde o primeiro ao último ano, que me deu os melhores conselhos e indicações, que nunca me falhou!

A todas e a todos as/os "Solidárias" que foram a minha família nestes últimos cinco anos, os companheiros de noites de estudo e de diversão. À Valéria a minha primeira amiga em Coimbra, à Sónia e à Joana que partilharam comigo os melhores e mais loucos momentos que vivi nesta cidade! Ao Edson, ao ph e à Inês pelo companheirismo. À Mafalda, a irmã que a faculdade me deu e que levo para a vida, por todas as conversas, conselhos, partilhas de experiências, jantares, por tudo…

À minha família de praxe que me acompanhou ao longo destes anos, com quem vivi as serenatas e todo o espírito de Coimbra!

A todas as pessoas que nestes 5 anos se cruzaram comigo e fizeram com que fossem os melhores anos da minha vida!

Aos meus amigos por toda a compreensão e apoio incondicional. À Guida, a minha melhor amiga e irmã do coração, pelos infindáveis telefonemas e horas de conversa, por todos os conselhos e amizade.

Aos meus vizinhos pelo apoio constante!

A toda a minha família que sei que sempre me apoiou e hoje está orgulhosa. À minha avó, que lá de cima tenho a certeza que me deitou a mão e esteve sempre comigo em todos os

momentos. Aos meus avós que apoiam cada conquista. À minha madrinha por toda a ajuda e preocupação. À minha irmã por todo o amor que sei que me tem.

Por último, mas sobretudo, aos meus pais! Sem eles nada disto era possível, sem eles nada conseguiria. Agradeço-lhes todos os esforços que fizeram, a motivação e apoio incondicional, o amor que sempre me deram!

A todos, o meu muito obrigada. Sem vocês nada seria possível!

Resumo

A Elastografia de Coerência Ótica (OCE) é uma técnica de imagem ótica que permite obter elastogramas: imagens em que os valores de cada pixel correspondem a medições das propriedades mecânicas da amostra. Esta técnica combina um sistema de excitação para induzir perturbações mecânicas com um sistema de tomografia de coerência ótica (OCT) para medir, ao longo do tempo, a resposta da amostra aos deslocamentos induzidos. A partir do mapa de deslocamentos, é possível visualizar a propagação de ondas mecânicas na amostra e obter imagens de propriedades mecânicas, tais como o módulo de Young.

Esta dissertação descreve a adaptação de um sistema OCE baseado num laser de fonte varrida (comprimento de onda central de 1040 nm), normalmente utilizado para aquisições oculares, para aplicações no campo da dermatologia.

O sistema desenvolvido utiliza OCT e é capaz de obter imagens tridimensionais do tecido e detetar o deslocamento da superfície através de medições sensíveis à fase: é utilizada a informação de fase obtida a partir do interferograma medido após a transformação de Fourier. Isto permite medir deslocamentos para diferentes profundidades da amostra, com uma resolução de nanómetros, cerca de 100 vezes melhor do que a resolução ótica do instrumento.

As propriedades mecânicas da pele podem-se alterar com diferentes fatores, tais como idade, localização, hidratação e patologias. Na medicina, a caracterização mecânica da pele é essencial para o diagnóstico de certas doenças, na avaliação de substitutos artificiais da pele, entre outros fins. Na indústria cosmética, a quantificação das propriedades mecânicas da pele permite provar as alegações dos fabricantes, tais como provar as propriedades rejuvenescedoras dos cremes anti-rugas e anti-envelhecimento.

Neste projeto, pretende-se avaliar a aplicação do sistema OCE desenvolvido na CIBIT para a medição das propriedades mecânicas da pele. Esta avaliação implica (i) a definição de protocolos de medição, (ii) a caracterização do sinal OCE gerado na superfície da pele e (iii) a medição quantitativa das propriedades cutâneas para diferentes condições, locais, tipos de pele, com e sem aplicação de produtos dermatológicos e cosméticos.

Abstract

Optical Coherence Elastography (OCE) is an optical imaging technique that allows obtaining images called elastograms in which the pixel values correspond to measurements of the sample's mechanical properties. This technique combines an excitation system to induce mechanical disturbances with an optical coherence tomography (OCT) system to measure, over time, the response of the sample to the induced displacements. From the displacement map, it is possible to visualize the propagation of mechanical waves in the sample and obtain images of mechanical properties such as Young's modulus. It is literally palpating with light!

This dissertation describes the adaptation of an OCE system based on a swept-source laser (central wavelength of 1040 nm), commonly used for ocular acquisitions, for applications in the field of dermatology.

The developed system uses OCT and is capable of obtaining three-dimensional tissue images and detecting surface displacement through phase-sensitive measurements: the phase information obtain from the measured interferogram after Fourier Transform is used. This allows measuring displacements for different depths of the sample, with a resolution of nanometers, about 100 times better than the optical resolution of the instrument.

The mechanical properties of the skin can change with different factors such as age, location, hydration and pathologies. In medicine, the mechanical characterization of skin is essential for the diagnosis of certain diseases, in the evaluation of artificial skin substitutes, among other purposes. In the cosmetics industry, quantification of the mechanical properties of the skin allows to prove manufacturers' claims, such as proving the rejuvenating properties of anti-wrinkle and anti-ageing creams.

In this project, we intend to evaluate the application of the OCE system developed at CIBIT to the measurement of skin mechanical properties. This evaluation implies (i) the definition of measurement protocols, (ii) characterization of the OCE signal generates at the skin surface and (iii) the quantitative measurement of the skin properties for different conditions, locations, skin types, with and without application of dermatological and cosmetic products.

List of Acronyms

OCE Optical coherence elastography

OCT Optical coherence tomagraphy

TD-OCT Time- domain optical coherence tomography

FD-OCT Frequency-domain optical coherence tomography

TD Time-domain

SD-OCT Spectral-domain optical coherence tomography

SS-OCT Swept source optical coherence tomography

MR Magnetic resonance

MRE Magnetic resonance elastography

MRI Magnetic resonance imaging

SNR Signal-to-noise ratio

EM Electron microscopy

SMR Shingled Magnetic Recording

AFM Atomic force microscopy

PhS-SSOCE Phase-resolved optical coherence elastography

UV Ultra-violet

SS Systematic sclerosis

BLM Bleomycin

FBG Fiber Bragg grating

FPGA Field programmable gate array

Ph Phantom

Sd Standard deviation

IQR Interquartile range

List of Figures

1. Introduction

Optical Coherence Elastography (OCE) is an emerging optical imaging technique to obtain images in which the pixel values correspond to measurements of the sample's mechanical properties. In this technique, an excitation system (by direct contact, ultrasound or compressed air blast) is used to induce mechanical disturbances combined with an optical coherence tomography (OCT) system to measure, over time, the sample's response to the induced displacements. From the displacement map, it is possible to visualize the propagation of mechanical waves in the sample and obtain images of the mechanical properties such as Young's modulus. It is literally palpating with light!

Contrary to traditional OCT applications in ophthalmology and cardiology, where the images are obtained from the amplitude of the Fourier Transform of the interference pattern, OCE uses the phase information obtained from the interferogram after using the Fourier Transform. This allows measuring displacements for different depths of the sample, with a resolution of tens of nanometers, about 100 times better than the optical resolution of the instrument.

At CIBIT we have developed an OCE system based on a swept-source laser source (central wavelength 1040 nm) with which we intend to study the applicability of this imaging modality in the field of dermatology.

The mechanical characterization of the skin is recognized as relevant in several fields namely in the medical and cosmetic fields. The mechanical properties of the skin vary according to several factors. The assessment of the change in the mechanical properties of the skin helps, for example, in the diagnosis and evaluation of therapeutic strategies. In the area of regenerative medicine, it is useful in the study of the healing and treatment processes of burns and in the evaluation of artificial skin substitutes. In the cosmetic industry, the quantification of the mechanical properties of the skin is very useful in proving the claims of manufacturers, such as the proof of the rejuvenating properties of anti-wrinkle and anti-ageing creams.

Throughout this project we verified the applicability of the OCE system in measuring the elastic properties of human skin, namely Young's modulus, and the changes observed in the skin after the application of an anti-aging cream. The difference between the elastic properties in different parts of the human body was also studied.

The structure of this dissertation is as follows:

- Chapter 1 presents an introduction to the research topic, its importance and the projects goals.
- Chapter 2 describes the OCT technique and its approaches in the time and frequency domain.
- Chapter 3 describes the OCE technique, delving into the phase-resolved OCE. A historical approach is also given.
- Chapter 4 describes in general terms the anatomy of the human skin.
- Chapter 5 presents the developments in elastography imaging techniques to date.
- Chapter 6 focuses on the OCE setup used in the CIBIT laboratory. Image acquisition and analysis protocols are described. The samples are also presented.
- Chapter 7 describes the preliminary experiments performed on phantoms and the *in vivo* experiments performed on humans.
- Chapter 8 presents conclusions and future work.

2. Optical Coherence Tomography

2.1. Principles of OCT

Optical coherence tomography (OCT) is a *in vivo* non-contact, real-time optical imaging modality. This optical imaging technique can produce high-resolution cross-sectional images of the internal structures of a sample by measuring the depth and magnitude of the retro-reflected light. OCT provides tissue images with a resolution down to a few micrometers and depths up to several millimeters, depending on the type of tissue [1].

This technique was first developed in 1991 in Fujimoto's laboratories [2] and was first used in 1993 to obtain *in vivo* images of the retina. The first OCT instruments became commercially available in 1996 [2] [3]. Although their clinical adoption has been slow, nowadays OCT is a standard of care in ophthalmology on pair with other major imaging modalities. OCT has also become very attractive in other medical and research applications such as dermatology. The first dermatology OCT product was developed in 2010 [2]. Investigations with OCT to assess skin structure in clinical settings have proven that this imaging method is useful in visualizing subsurface structures of normal skin, including the epidermis, dermo epidermal junction, dermis, hair follicles, blood vessels and sweat ducts [1] [4].

The main piece in the design of the OCT system is an interferometer using a source with low temporal coherence producing a collimated laser beam [3]. Light passes through a beam splitter and is split into two beams: one beam passes through the splitter; the other is reflected in a perpendicular direction. These beams are reflected by mirrors and return to the beam splitter, where they interfere and are directed towards the detector [5]. If the general paths taken by the light beams differ slightly in length a fringe pattern can be seen on the detector. This pattern occurs due to constructive and destructive interference between both beams, which are similar in almost all respects, but which are out of phase [6].

A simple Michelson interferometer as shown on Figure 1, consists of a detector and two arms: the sample arm and the reference arm. The sample arm contains a modular probe that focuses and sweeps light onto the sample and the reference arm is equipped with a mirror [6]. The field of the reference beam coherently matches the sample field of the arm and

interferes to form fringes. A detector measures the output intensity which is proportional to the square of the electromagnetic field [4] [7].

In OCT, backscattered photons from a tissue of interest within a coherence length of the source using a two-beam interferometer are detected [8]. This image mode can take different configurations. OCT imaging modalities are divided into several concepts. The most important techniques are OCT in the time-domain (TD-OCT) and in the frequency domain (FD-OCT). The details of the implementation in both the cases are described below [4] [7].
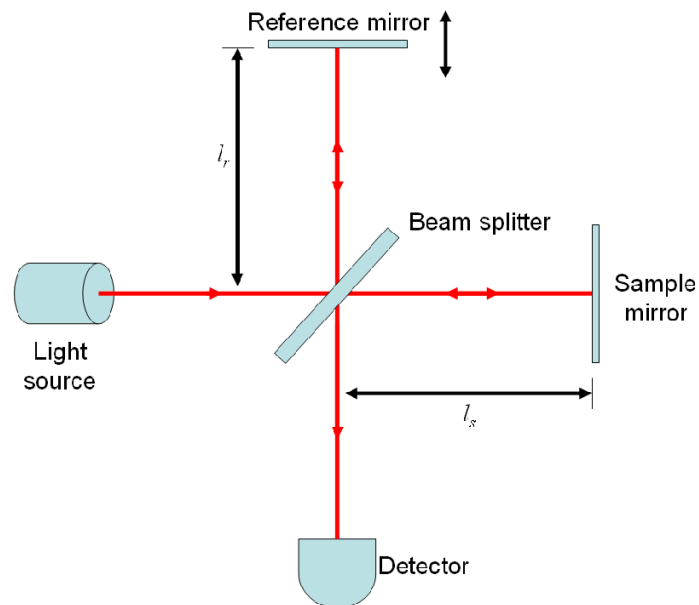
Figure 1 Diagram of a typical Michelson Interferometer; ls- wavelength waves reflecting from the sample arm; lr- waves reflecting back from the reference arm reference arms [6].

2.2. TD-OCT

In OCT system with two arms the backscattered light coming from the sample arm recombines with the light in the reference arm resulting in fringe formation. The distance travelled by the light in both arms do not differ by more than the coherence length of the laser source [7].

The first OCT systems were based on TD techniques [6]. A schematic representation of a TD-OCT is shown on Figure 2. In the time-domain configuration, the reference arm is equipped with a trans-attenuating mirror which is not stable but moves while the sample arm remains static. This leads to a variation in the echo delay required to extract axial data (A-scans) from the analyzed sample [2] [7].

The coherence length of light determines the distance between two points in space where interference is possible. The interference phenomenon occurs when the path difference is smaller than the coherence length of the source. In this way, the path length of the reference beam is varied, allowing interference with reflections from different scattering surfaces on the sample [2]. The backscattered photons from each depth are obtained at different times with the movement of the mirror encoding the information time [7].

Information about the sample structures can then be obtained from the photodetectors that record the interference signals. The interference data is recorded at points across the surface. The galvanometric mirror allows the information to be digitized to construct, real-time, 2-D cross-section (B-scans) and volumes [2] [7].
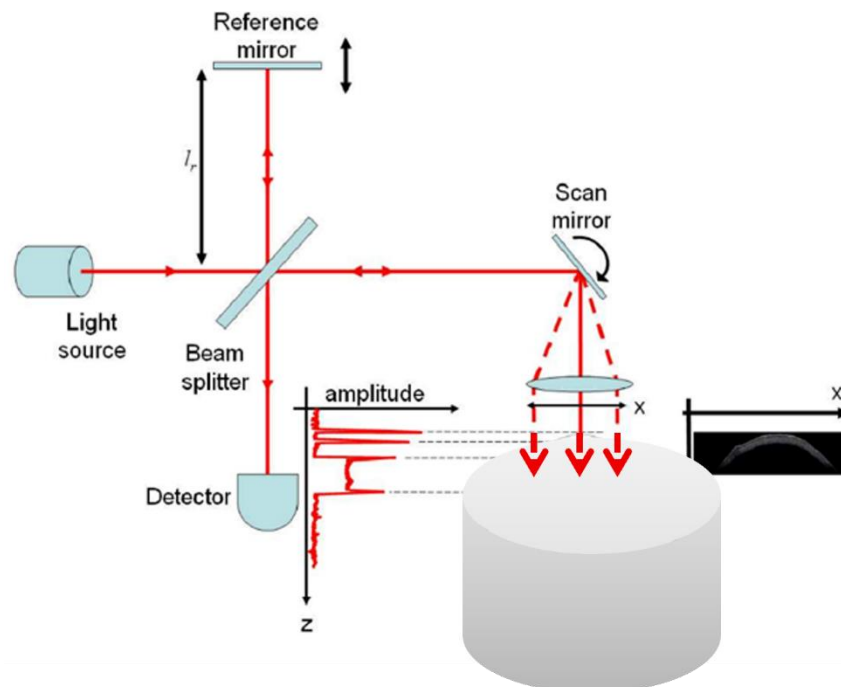
Figure 2 The schematic of convencional TD-OCT (adapted from [6]).

2.3. FD-OCT

After TD-OCT, new OCT configurations began to emerge. Frequency domain techniques do not require deep mechanical scanning and have a higher detection sensitivity compared to TD-OCT, allowing OCT imaging with a high increase in imaging speed [9] [10].

In an FD-OCT system different wavelengths of the broadband source probe at different depths and the depth information are spectrally encoded and recorded by the spectrometer. This signal is then Fourier transformed. The A-scans correspond to the complete depth

profile of the reflectivity of the sample at the beam position (amplitude scan). In a typical FD-OCT system, axial depth reading can be performed by scanning the spectrometer's diode array. In the frequency domain, there are two main approaches where the mirror on the reference arm is fixed: Spectral Domain OCT (SD-OCT) or Swept Source OCT (SS-OCT) [2] [11].

The Fourier transform also provides information on the phase spectrum which is often used to extract mechanical properties of a sample (with a piezoelectric vibrating actuator on top, for example) with the phase-sensitive approach. This technique is called Optical Coherence Elastography [2].

2.3.1. SD-OCT

In SD-OCT, the detector is replaced by a spectrometer with a multi-channel analyzer. Spectral domain detection techniques measure the echo time delay of light using an interferometer with a broadband light source and measure the spectrum of the interferometer output. Light that is backscattered from different depths in the tissue and superimposed on the light from the reference arm modulates the spectrometer with a frequency directly proportional to the depth of the tissue structures [6].

The signal obtained (the light from the tissue) in frequency is transformed into a signal in the time spectrum by the Fourier transform and so we have direct access to the depth information as shown in Figure 3 [2] [7].
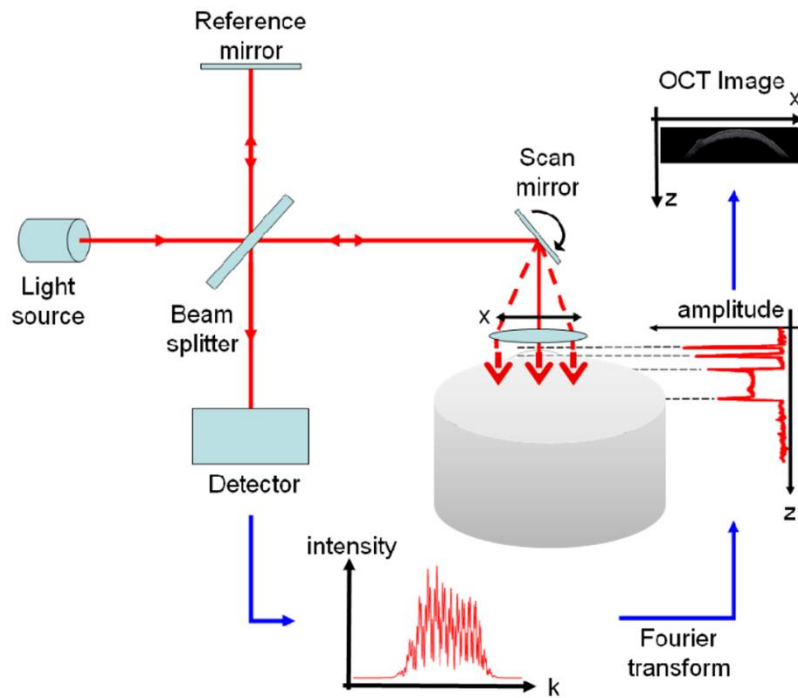
Figure 3 The schematic of conventional SD-OCT (adapted from [6]).

2.3.2. SS-OCT

The second FD-OCT approach is swept-source OCT (SS-OCT). Unlike SD-OCT it uses a fast tuning, narrow linewidth laser source. Typically, SS-OCT systems are composed of swept laser source that scans the wavelength of the spectrum over a time interval, an interferometer and signal processing tools. The detector is a simple photodiode that allows high-speed detection and produces a signal that is acquired for one wavelength at a time [2][3].

While the laser is scanning over a wavelength range the detector records an A-scan. Through Fourier transform we obtain depth information which allows us to obtain the amplitude spectrum. This corresponds to the axial reflection information of the sample recorded data and is equivalent to the data recorded by the spectrometer in SD-OCT. Thus, an axial reflection profile, which is ultimately a function of the refractive index distribution along the depth of the sample [2].

Figure 4 shows a typical SS-OCT system where we can observe (A) the interferometer with swept laser source and beam splitter and path difference ΔL, (B) the time delay of the sample light (dotted) and the reference light (dashed), the (C) Interference signal

proportional to the delay and finally (D) the Fourier Transform of the interference signal measures ΔL [12].
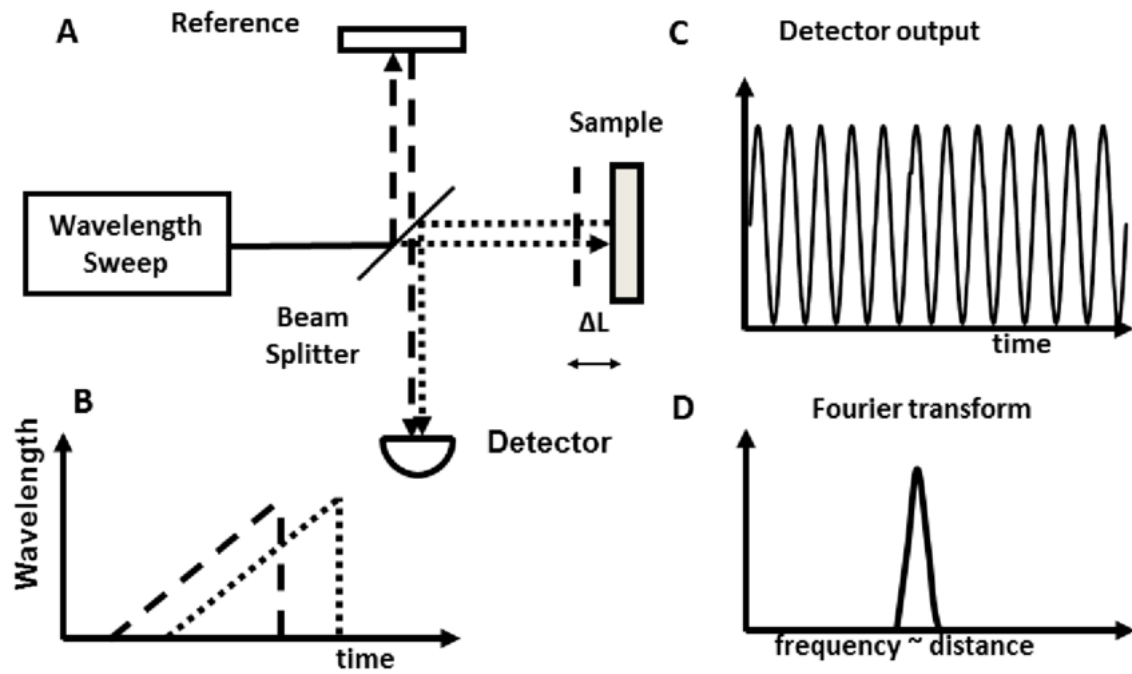
Figure 4 The schematic of conventional SS-OCT (A), the delay of the sample and reference light (B), interference signal (c) and Fourier transform (D) [12].

3. Optical Coherence Elastography

Optical coherence elastography (OCE) is an emerging imaging modality that allows measuring mechanical properties of a sample by optical interference. OCE combines optical coherence tomography (OCT) to detect tissue motion with an excitation source to induce tissue displacement. Through OCE it is possible to retrieve information such as the wave propagation velocity and infer on the tissue Young's modulus [13].

3.1. OCE history and features

Palpation has played an important role in patient's examination since the 18th century. Through palpation it was possible to assess tissue's physical characteristics and mechanical behavior [14]. Currently, estimation of tissue elasticity or rigidity can be performed with higher accuracy by elastography. The first definition of "elastography", as the mapping of local mechanical properties of tissues, using medical imaging to measure the deformation in response to mechanical loading, dates back to 1979 [15]. At this time the tissue movement was characterized by determining the decorrelation time rate between successive collinear A-scans made through the tissue volume of interest. Studies conducted by the Mount's group by Maria Tristan and Jeff Bamber have shown that the decorrelation time rate between successive A-scans can be a useful discriminator between hard and soft tissue subject to secondary or externally induced motion. Tristan and co-workers were able to discriminate normal liver parenchyma from liver metastases using a multidimensional evaluation of Fourier coefficients associated with cross-correlation. These pioneering studies were rooted in ultrasonic elasticity imaging [16]. Since then, its applications have increased extensive, particularly in combination with magnetic resonance imaging and ultrasound [15]. Elastography allied to magnetic resonance (MR) and ultrasound techniques have come into use as a diagnostic tool for a considerable number of diseases, such as the detection of cancerous lumps in the breast or prostate [15] [17].

The first MR elasticity experiments were performed by R. Buxton and A. Sarvazyan [16] on a phantom mimicking soft tissue with inclusions. Mathematical analysis of the MR data on the deformation of inclusions showed that liquid-filled capsules with their complex structure provided local deformation effects. Homogeneous inclusions were detected with Young's modulus values two times smaller than those of the surrounding material. Between 1995 and 1996, a collaborative study conducted at the University of Michigan Laboratories

and Artann was able to demonstrate for the first time the use of MR imaging to record shear wave propagation [16].

Subsequently came magnetic resonance elastography (MRE), based on phase contrast magnetic resonance imaging (MRI) that measures mechanically induced propagating acoustic waves in tissue. Both techniques have been widely developed and applied clinically, but have some limits related to spatial resolution and signal-to-noise ratio (SNR) of tissue displacement. The spatial scales for elasticity imaging remain at the macroscopic level with the field-of-view of the organ size for electron microscopy (EM) and the typical resolution of hundreds of micrometers and several millimeters for Shingled Magnetic Recording (SRM) [16].

An alternative method is to use atomic force microscopy (AFM) based elastography. This technique is used to probe the mechanical properties of a single cell by applying nanoscale indentation, provide the contact force at the sub-nanonewton level to load the cell membrane, and measure the induced deformation with sub-nanometer precision. These AFM elastography features have contributed to several studies on cell mechanics and cell biology and cell pathology detection [1] [18].

Different spatial scales of mechanical assessment are essential for understanding various physiological states and detection of tissue-specific pathologies, and it's important to have an imaging technique that can bridge the imaging scales gap between elastography AFM (cellular level) and ultrasound/MR (organ level). In this view, optical techniques have been proposed for elastography, allowing the probing of tissue mechanical properties with optics [15] [16].

The use of optics offers an improvement in features such as imaging spatial resolution, acquisition speed, mechanical sensitivity, and imaging penetration, when compared to ultrasonic elastography and MRE. OCE is a form of palpation with light and represents the frontier of optical elasticity imaging techniques and focuses on the micro-scale assessment of tissue biomechanics in 3D that is hard to achieve with traditional elastography methods [1] [15].

OCE was first proposed and demonstrated in 1998 by Schmitt *et al* [3]. They employed OCT to detect sample deformations with depth resolution induced by quasi-static compression. The resulting local displacement field was analyzed through the correlation between transverse (B-) scans of the same location. The results were used to produce

elastograms [16] [19]. Schmitt's work emphatically demonstrated that the OCT could be used to obtain information about the mechanical properties of a soft tissue and measured local displacement and inferred strain. Strain is a relative quantity related to an absolute quantity, an elastic modulus or Young's modulus.

The first OCE application was based on the operation of a TD-OCT system (described in section 2.2). Its principle of operation was initially based on internal displacements indicating the biomechanical properties of the samples based on 2-D cross-correlation algorithms. This method had a displacement sensitivity equivalent to that of the OCT system used. This was followed by dynamic OCE using an external mechanical stimulus (a piezoelectric ring) and a TD-OCT system based on a Bessel frequency spectrum of the interferometric OCT signal. In 2007 Fourier domain OCT systems started to be widely used and the phase sensitive OCE method (described below) was introduced [20].

3.2. Principles of OCE

OCE is a novel elastography technology that combines an excitation system, to induce mechanical disturbances, with *in vivo* imaging OCT. A schematic representation of the principle of operation of an OCE in show Figure 5. When compared with other elastography techniques, OCE [15]:

- OCE allows to obtain images with a much higher spatial resolution (in the order of nm).
- Has acquisition rates far superior allowing for *in vivo* 3D elastography imaging.
- Has a sub-nanometer resolution sensitivity that allows us to measure displacement and mechanical changes in the skin that would not be detected otherwise.

For these reasons, OCE is seen as a potential solution for measuring mesoscopic mechanical properties in dermatology.

One drawback of OCE is that its penetration into the tissue is also much lower when compared to ultrasound and MRI elastography. However, this is not a problem, the benefits of this technique are much more relevant [15].
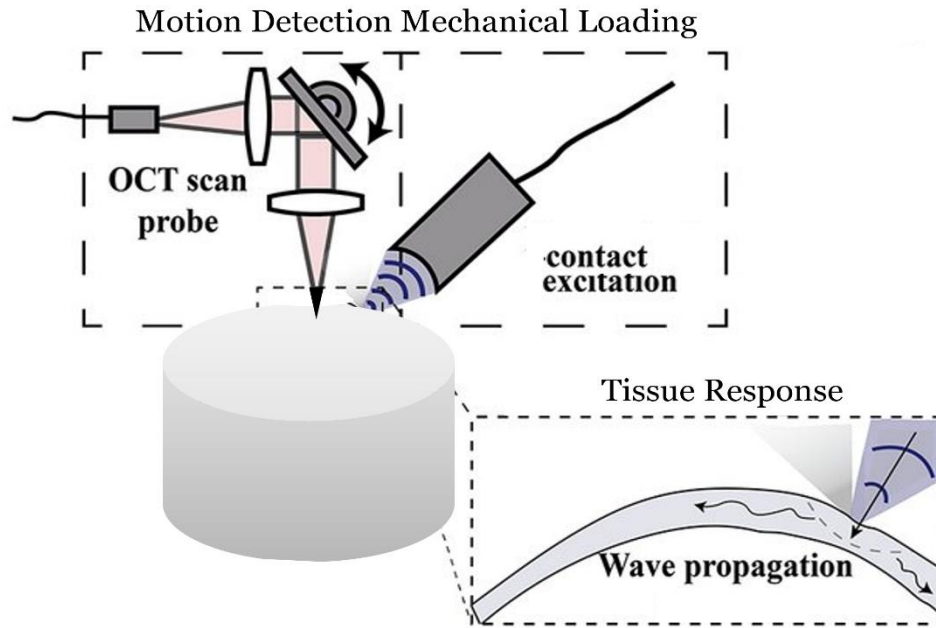
Figure 5 Schematic demonstrating the main components of OCE (adapted from [21]).

3.2.1. Phase-resolved OCE

Techniques based on phase information in the imaging field allow the retrieval of optical phase at low coherence interferometry and quantification of refractive index variations. Phase resolution allows sub-pixel image analysis [21].

PhS-SSOCE consists of excitation unit (in our case a piezoelectric attenuator), detection unit and data acquisition unit. The piezoelectric attenuator induces mechanical vibrations on the surface. The amplitude of these vibrations is subsequently measured by the sensing unit. The amplitude vibrations are achieved by taking M-mode images at spatially distributed points on the surface. The data is recorded using the data acquisition unit which is also responsible for providing synchronization between the detection unit and the excitation unit.

The phase-resolved OCE method, when compared with other ways to detected displacements, is more sensitive to small displacements of scatterers in the tissue, providing sub-nanometer displacement sensitivity [20].

In phase-resolved OCE, the phase difference, $\Delta\varphi$, at each depth z, is computed as the difference between the phase of two consecutive A-scans ($\varphi 1(z)$ and $\varphi 2(z)$) acquired at the same lateral location [15]:

$$\Delta\varphi(z) = \varphi2(z) - \varphi1(z) \ (1)$$

The displacement Δd is correlated with the phase difference, $\Delta\varphi$ as:

$$\Delta d = \Delta\varphi \ \frac{\lambda_0}{4\pi n} \ (2)$$

where, λ_0 is the central wavelength of the laser, and n is the sample's refractive index.

Due to its resolving power and sensitivity, phase resolved OCE skin imaging has been increasingly used to distinguish between different tissue types [20].

3.2.2. Wave based OCE

The induction of an axial displacement by a mechanical pulse produces Rayleigh waves and other mechanical waves as we can see on Figure 6 (a). An isotropic, elastic solid material supports two types of waves inside, bulk waves. These waves are independent of boundary conditions as the wave speed is directly related to the mechanical properties of the medium where it propagates. Bulk waves can be classified with respect to the direction of vibration into transversal and longitudinal waves. In a transverse wave the vibration made to produce the wave is perpendicular to its direction of propagation. Transversal waves are also known as shear waves. In longitudinal waves, also called compressional waves, the particles oscillate in a direction perpendicular to the direction of propagation of the wave [22] [23].

The mechanical wave (displacement vector $\vec{U}$) propagating inside the material can be represented as the sum of the longitudinal $(\vec{U_l})$ and shear $(\vec{U_s})$ displacement components:

$$\vec{U} = \vec{U_l} + \vec{U_s} \ (3)$$

Longitudinal and transverse waves obey independent equations of motion and the velocities of propagation of these waves are respectively given by:

$$C_l = \sqrt{\frac{(\lambda+2\mu)}{\rho}} \ (4) \text{ and } C_s = \sqrt{\frac{\mu}{\rho}} \ (5)$$

Typically, only shear waves are considered in OCE because in an almost incompressible medium the propagation speed of longitudinal waves is much higher than the speed of shear probes. Considering only shear waves is more convenient in studies of the elasticity of the medium for several reasons: the speed of shear waves depends only one *Lamé* constant;

when the measurable shear waves start propagating the longitudinal waves have already reached depths unreachable with OCT.

Figure 6 (b) depicts the different mechanical waves generated when a harmonic axial load is applied to the surface of a semi-infinite elastic medium. Colormap represents the normalized displacement magnitude in arbitrary units [22].
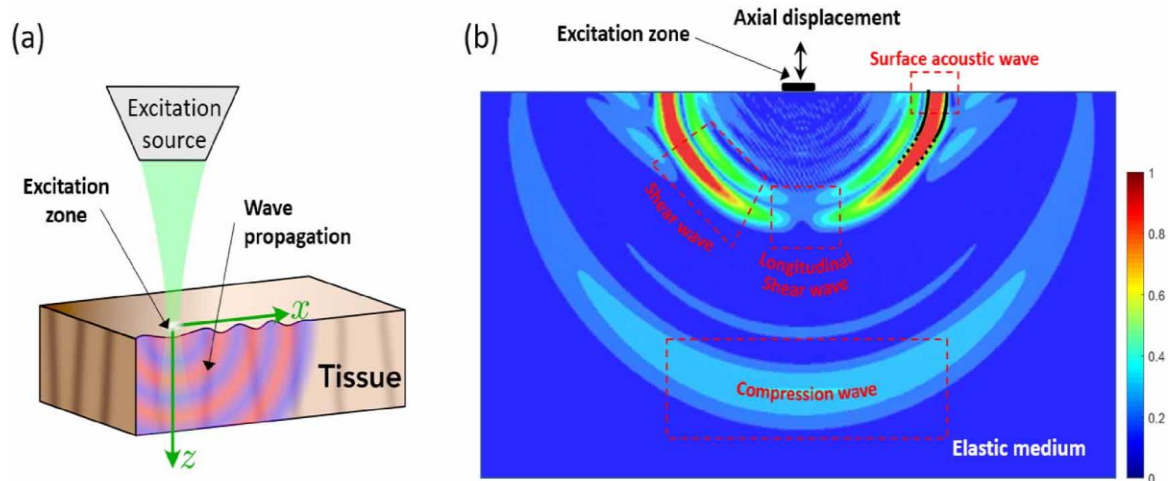
Figure 6 Mechanical waves: direction of propagation in (a) the tissue and (b) mechanical waves in an elastic medium (b) [24].

In addition to bulk waves there are surface waves. These waves propagate along a free surface or along the boundary between two different solid media. Rayleigh waves are a type of surface wave that propagate along the surface of a semi-infinite elastic solid. They are formed when the motion of the particles is a combination of longitudinal and transverse vibration giving rise to an elliptical retrograde motion in the vertical plane along the direction of travel [24].

4. Human skin anatomy

Skin is the largest organ of the human the body and together with derivative structures (hair, nails, oil glands and sweat glands) make up the integumentary system. It performs many vital functions including protection against aggressions since the structure of the skin is made up of an intricate network that serves as the body's initial barrier against pathogens, UV light, and external physical, chemical, and mechanical injuries. It also helps in regulating body temperature and preventing excessive water loss. The nerves in the skin are responsible for feeling sensations such as heat and cold [1].

The skin is composed of 3 main layers: dermis, epidermis, and hypodermis (subcutaneous tissue) as shown in Figure 7. Each layer is made up of different cells that carry out different functions. The epidermis, the outermost layer, is mainly composed of cells known as keratinocytes because of their ability to produce keratin. The dermis is the middle layer and is made up of elastin and a protein structure known as collagen. The hypodermis is the innermost layer and contains small cells called lipocytes [25][26]. The characteristics of each layer are discussed in more detail below.

The thickness of each layer of the skin varies considerably depending on the region of the body and is categorized based on the thickness of the epidermal and dermal layers.

There are two main kinds of human skin: non-hair skin and hair-bearing skin. The non-hair skin or glabrous skin is thicker because the epidermis contains an extra layer, the stratum lucidum and can be found on the palms and soles of the hands. It is characterized by a thick epidermis with many layers, by a dermis with encapsulated sense organs and a lack of hair fluids and sebaceous glandules. On the other hand the hair-bearing skin is composed by encapsulated sense organs, hair fluids and sebaceous glandules [25].
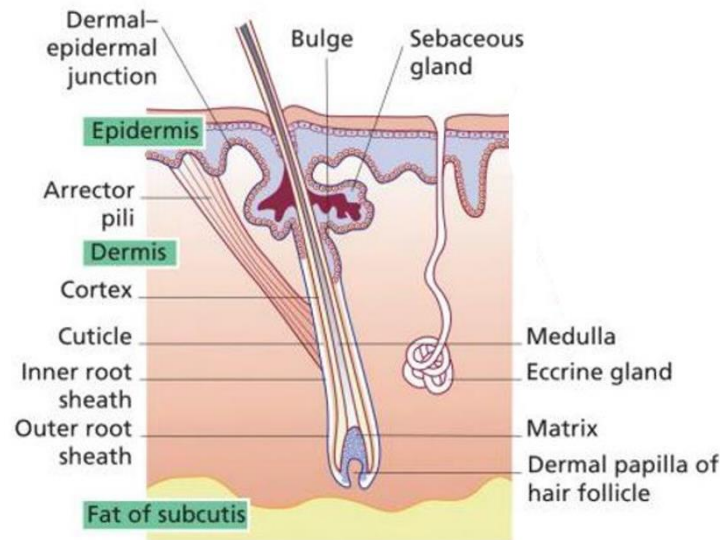
Figure 7 The structure of the skin (adapted from [25]).

4.1. Epidermis

The epidermis is a stratified, avascular, squamous layer of epithelium as shown in Figure 8. It consists mainly of two types of cells: keratinocytes and dendritic cells. The epidermis also houses several other cell populations, such as melanocytes, Langerhans cells, and Merkel cells, although keratinocytes are the most abundant population (around 80% of cells in the epidermis are the ectodermal derived keratinocytes) [25] [27]. It is important for skin hydration, wound healing, and aging [28].

Keratinocytes originate from the basal layer. As the cells migrate from the basal layer to the surface of the skin the differentiation process occurs which results in keratinization. In this process, the keratinocyte first undergoes a synthetic phase and then a degradative phase. In the synthetic phase, the cell builds a cytoplasmic supply of fibrous keratin filaments whose bundles converge and terminate at the plasma membrane forming the intercellular attachment plates known as desmosomes. In the degradative phase these plates and organelles are lost, and the cell contents are consolidated into a mixture of filaments and amorphous cell envelopes. The final cell that results from this process is called a corneal cell [25] [27].

Melanocytes are dendritic cells originating in the neural crest that form melanin by the action of the enzyme tyrosinase. Langerhans cells are mobile dendritic cells of the mononuclear phagocytic system that recognize, process and present antigens to some

specific lymphocytes. Merkel cells are found in the basal layer and are of neuroectodermal origin [25].

The epidermis is divided into 5 sub-layers: stratum basale, stratum spinosum, stratum granulosum, stratum lucidum, and stratum corneum [27].

The basal layer, also known as the stratum germinativum, is a single layer of small, cuboidal cells that rests on the basal lamina. It contains keratinocytes that progressively become low columnar and have less cytoplasm than the cells above. These basal cells have large amounts of melanin pigments, desmosomes and hemidesmosomes [25] [27].

The spinous layer is composed of 5 to 15 layers of cells that differ in shape, structure and subcellular properties, depending on their location. These cells have several cytoplasmic extensions joined to those of neighboring cells by desmosomes that promote mechanical coupling between epidermal cells and provide resistance to physical stresses [25].

As one moves up the layer the size of the cells increases, and their shape becomes flattened parallel to the surface. The lamellated granules, keratinosomes, or Odland bodies, rich in glycolipids and sterols, appear in the upper zone of the spinous layer when the keratinocytes start producing keratohyalin granules. These granules assume an important role in the production of an epidermal water barrier and in the conversion of tonofilaments into keratin. In this layer, the keratinocytes are already larger than in the basal stratum [25].

The granular layer is the most superficial layer and is a very basophilic zone with the thickness of 1-3 layers of flattened cells. The keratinocytes have keratohyalin granules rich in cystine and histidine proteins. These keratohyalin granules contain keratin precursors that eventually aggregate, crosslink, and form bundles being responsible for further synthesis and modification of proteins involved in keratinization. The lamellar granules contain the glycolipids that secrete to the surface of the cells and act as a glue, holding the cells together [25] [27].

The stratum lucidum is a layer that only appears on thick skin found on the palms of the hands and soles of the feet. The cells present in this stratum have lost or are losing their nuclei and are eosinophils with the advanced state of keratinization [27].

The cornified layer consists of flattened, anucleate, desiccated cells (dead keratinocytes) which provide mechanical protection for the underlying epidermis and a barrier to prevent

water loss and invasion by foreign substances. The cytoplasm of these cells has been replaced by keratin filaments [25].

The desquamation of the epidermis is regulated by proteolytic activity which acts at the level of the desmosomes. Thus, the serine peptides, responsible for this regulation, act when the pH drops degrading the desmosome junction [25].
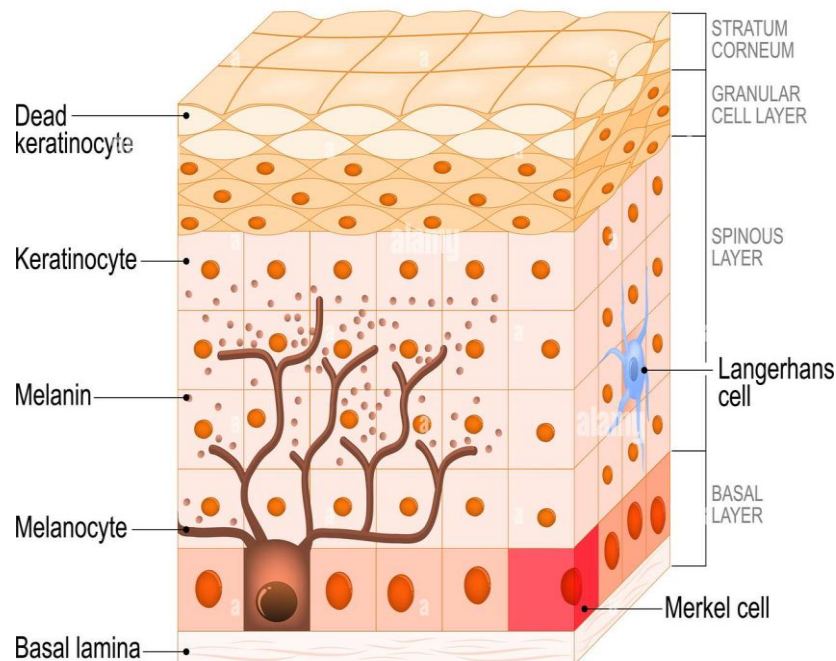
Figure 8 The structure of the epidermis skin (adapted from [25]).

4.2. Dermis

The dermis is aligned to the epidermis through the basement membrane and comprises most of the skin thickness. It is composed of two sub-layers of dense, fibrous, filamentous, amorphous connective tissue that accommodates stimulus-induced input from nerve and vascular networks, epidermally derived appendages, fibroblasts, macrophages, and mast cells: the papillary layer and the reticular layer [25] [29].

This layer is responsible for the suppleness, elasticity, and tensile strength of the skin protecting the body from mechanical injury. It binds water that helps in thermal regulation, and it includes receptors for sensory stimuli. The dermis interacts with the epidermis in maintaining the properties of both layers [25].

The papillary layer is the most superficial sub-layer of the dermis and consists of non-ordered lax tissue with 3D fibers, with a predominance of collagen type I and III and elastic.

It contains nerve endings and blood vessels, mainly in the dermal papillae that increase adhesion to the epidermis [25].

The reticular layer is thicker and less cellular than the papillary layer. It is composed of dense connective tissue with abundant collagen I and eulauninic and common elastic fibers, organized in the form of Langer's lines (regular lines of cutaneous tension) [25].

Deeper within the reticular layer there may be smooth muscle with a thermoregulatory function [25].

4.3. Hypodermis

The hypodermis is innermost layer of the dermis and is also called the subcutaneous fascia. It is composed of loose connective tissue, adipose tissue and small clusters of smooth muscle that form the erector capillaries. It also contains some skin appendages such as hair follicles, sensory neurons, and blood vessels [25].

This sub-layer is considered by some authors to be an endocrine organ that provides the body with buoyancy and functions as an and functions as an energy store.

5. State of art of OCE skin imaging

Although OCT is most used in clinical practice to image the human eye, dermatology is also an important and relevant field of application. In fact, in recent years, skin examination in healthy and disease using OCT has drastically increased and several new clinical devices have been developed. Research using OCT has proved that this imaging modality is very useful in visualizing the structures of the skin and different organs. The accuracy of OCT technology, in its different technical variants, is also very useful in the diagnosis and monitoring of skin diseases, including malignancies and inflammatory conditions [4].OCE is used to determine tissue biomechanics and it is also seen as a potential solution for measuring mesoscopic mechanical properties in dermatology [4]. To fully characterize the tissue as a mechanical system, many parameters are required including shear and Young's modulus, bulk compression modulus, frequency dependencies of these moduli, nonlinearity, Poisson's ratio, viscosity, poroelastic parameters, anisotropy, and heterogeneity indices, etc. However, in most practical cases, only one elasticity parameter is used: Young's modulus which corresponds to the common terms "elasticity" or "stiffness". Young's modulus have a significant dependence on structural changes in the tissue [16].

The mechanical characterization of the skin is recognized as relevant in several fields, including medicine and the cosmetic industry. The mechanical properties of the skin vary with age, location, hydration, among other factors. They are useful in the diagnosis and evaluation of therapeutic strategies, in the study of healing processes, in the classification of burn scars and in the evaluation of the quality of artificial skin substitutes and the definition of surgical incision lines [4].

In cosmetics industry, quantification of the mechanical properties of the skin is very useful in proving manufacturers' claims, such as proving the rejuvenating properties of anti-wrinkle and anti-aging creams. Currently cosmetic manufacturers are also required by law to provide scientific evidence of the properties they advertise for their products. When evaluating skin care products for human skin, quantitative testing methods need to be simple, accurate and reliable. The efficacies of products for wrinkle reduction are usually assessed qualitatively by macroscopic analysis, microscopy, and subjective tools such as questionnaires. However new quantitative techniques, like OCE, are being adopted. Vasquez Pinto *et al.* proved in a study that by using the OCT, it was possible to quantify

the changes in skin roughness and the distribution of skin wrinkles in depth, with adequate sensitivity [30]. In this study, the authors used a commercial OCT device to perform clinical examinations of the skin roughness. The volunteers applied a commercially available anti-ageing cream for 28 days. Measurements were taken on days 0, 7, 14 and 28 of treatment at treated and untreated sites in the periorbital region. OCT allowed direct visualization of the skin topography with micrometer resolution, a reliable and interactive tool for clinical use and to check the efficacy of cosmetic products in real time [30].

As already mentioned, OCE is a rapidly emerging technique that allows to assess mechanical contrast in tissues with micrometer spatial resolution and therefore some applications in medicine are beginning to emerge [1]. One of the applications is the quantification of skin disease in systematic sclerosis (SSc). In a work carried out by Young Du *et al*, OCE was applied to assess the mechanical properties of skin in both controls and bleomycin (BLM) induced SSc-like disease non-invasively. In *in vivo* and *in vitro* studies, it was found that the Young's modulus of BLM-SSc skin is significantly higher than that of normal skin. Thus, through OCE it was possible to differentiate healthy and fibrotic skin using mechanical contrast and quantify skin involvement in SSc in a rapid, unbiased, and non-invasive manner [31]. Another proved application was the measurement of heterogeneous tissue with both tumor and adipose regions and to spatially map different biomechanical regions in human tissue with microscale resolution [15].

External dynamic OCE using surface wave propagation is a way of measuring the biomechanical properties of the skin. Xing Liang *et al.* used this OCE technique to measure the Young's Modulus under different driving frequencies and skin hydration conditions. In this study, a mechanical-wave driver was used for external mechanical excitation synchronized with an SD-OCT system for the detection of surface wave propagation on the skin. In the acquisition protocol an initial distance between the OCT sample arm beam and the mechanical waveguide was arbitrarily established. An M-mode OCT image was recorded at the first position and then the sample arm beam was moved a certain distance away from the mechanical wave conductor before the next image was taken. Acquisitions were made at various imaging positions per step to average the data from each measurement. The phase data from the OCT images were used for skin displacement detection. Using the phase data, the surface wave velocity and consequently the Young's modulus were calculated. All *in vivo* experiments were performed on the skin of a healthy male volunteer in the regions of the volar forearm, dorsal forearm, and palm. A hydrated

skin condition was produced by immersion of normal skin in a water bath for 20 minutes, followed by topical application of glycerin for 10 minutes. A dehydrated skin condition was produced by passing heated air from a commercial hair dryer over normal skin for 30 minutes. From this study the authors concluded that the results depend on the frequency of dynamic OCE measurements on human skin. The moisturizing process tended to increase the stiffness of the skin in the epidermis and dermis layers, since the measured Young's moduli increased when the driving frequency increased. For dehydrated skin, the Young's modulus was higher than that of normal skin under a conduction frequency of 50Hz, but for higher frequencies, the measured Young's moduli remain similar to those of normal skin [13].

Xing Liang *et al*. conducted other study that showed that information about the biomechanical properties of *in vivo* human skin could be obtained with their OCE system. The acquisitions were performed on the skin surface of volunteers in three different areas: volar and dorsal forearm and palm. For the data analysis they used an algorithm that considered the skin a model of an elastic and homogeneous infinite layer. In this work, using OCT, they obtained information about skin thickness. Through B-scan images they were able to access features of the human skin structure. The different regions in which images were obtained showed different thickness of the stratum corneum. For OCE measurements MB scan was used to obtain volumes. With these data and using algorithms they obtained the wave propagation speed at the surface and consequently Young's modulus. Different skin sites had different values for Young's modulus [32].

With the work presented in this MSc thesis, we further contributed to the demonstration of OCE applicability in dermatology. We evaluated skin elastic properties in different skin areas (volar and dorsal forearm and palm) and assessed the influence of subject gender on the skin elastic modulus. Moreover, we investigated the influence of anti-aging creams the skin elastic modulus. To the best of our knowledge, we present the first results on anti-aging cream efficiency evaluation using OCE.

6. **Material and Methods**

6.1. OCE Setup

A schematic representation of OCE system used in this study is shown in Figure 9. It consists of a SS-OCT combined with piezoelectric actuator to induce tissue displacements. The swept-source laser of the SS-OCT outputs the laser beam and eletrical signals: the clock signal. The laser output is split by a 90:10 fiber coupler where 10% of the light goes to the fiber Bragg Grating (FBG) and the remaining 90% to the system arms. FBG allows block certain wavelengths, behaving like an in-line optical fiber, or it can be used as a wavelength-specific reflector [33]. In this SS-OCT system, the FBG is used as a specific reflector reflecting light with a wavelength of $990 \pm 1\ nm$. The light reflected by the FBG is converted into an electrical signal by a photodiode and directed to a digital delay and pulse generator (DG535, Stanford Research Systems, California, USA) to generate trigger pulses with time and amplitude suitable for data acquisition.

The light passing to the system arms is split: 90% to the sample arm and 10% passes through a fiber polarizer and goes to the reference arm to generate the interferograms. The fiber polarizer removes the polarization differences between the two arms. We use in-line fiber optic polarization controllers from Thorlabs. The principle behind this is that while applying pressure and rotation on the fiber a linear birefringence is induced. The pressure applied creates a fiber wave plate, which slows down the signal and, combined it with the squeezing rotation, causes the birefringent portion of the fiber to also rotate, changing the polarization [34].

The light is directed into the sample arm using a 50 to 50 fiber coupler. The light arriving at the reference arm is reflected from a stationary reference mirror exiting through a collimator. The collimator reduces surface reflections and transmits most of the signal of interest. This signal is directed to a 50 to 50 coupler. At the sample arm, the light is focused onto the sample via a collimator and is directed to a galvanometric control system which moves narrow laser beams with accuracy, speed, and precision. The beam is focused on the sample after passing through two lenses (LA1131-AB and LA1131-B, Thorlabs Inc. Newton, New Jersey, United States). The reflected light then follows the reverse path until it reaches the 50 to 50 coupler. The resulting interference fringes, formed by coupling the sample and the reflected reference light using a 50 to 50 optical fiber couple, are detected

using a balanced photodetector. The photodetector subtracts the two signals to remove common mode noise. In our setup the Thorlabs' Balanced Amplified Photodetector PDB471C is used. This photodetector consists of two balanced photodiodes and an ultra-low noise, high speed transimpedance amplifier. The combination of the two photodiodes allows to achieve an excellent common mode rejection ratio, leading to better noise reduction [35].

The photodetector output is digitalized by an DAQ board that also receives signals from the clock and the FBG-generated signals as trigger. These signals control the acquisition of each individual sample, signaling the correct times for acquisition and providing information on the wavelength emitted by the source.

The DAQ board (X5-400M, Innovative Integration, Inc., Indianopolis, USA) is responsible for acquiring the analogue electrical signals, converting them into digital signals and sending them to a computer for further processing. This completes the process for acquiring an A-Scan. Additionally, the inverted signal of the FBG transmission, equivalent to the FBG-generates trigger, is recovered into a second channel of the DAQ board for post-processing jitter corrections.

The displacements were induced using a piezoelectric actuator (P-287, Physik Instrument, GmbH & Co. KG, Karlsruhe, Germany). The tip of the contact rod is circular with a diameter of about 1.3 mm. Mechanical vibrations were triggered by a transient pulse signal synchronized with the galvanometric mirrors and the FBG-generated trigger to initiate data acquisition using a custom field programmable gate array (FPGA). The width, delay and amplitude of the transient pulse signals were controlled using an arbitrary function generator (AFG3101C, Tektronix, Oregon, USA).
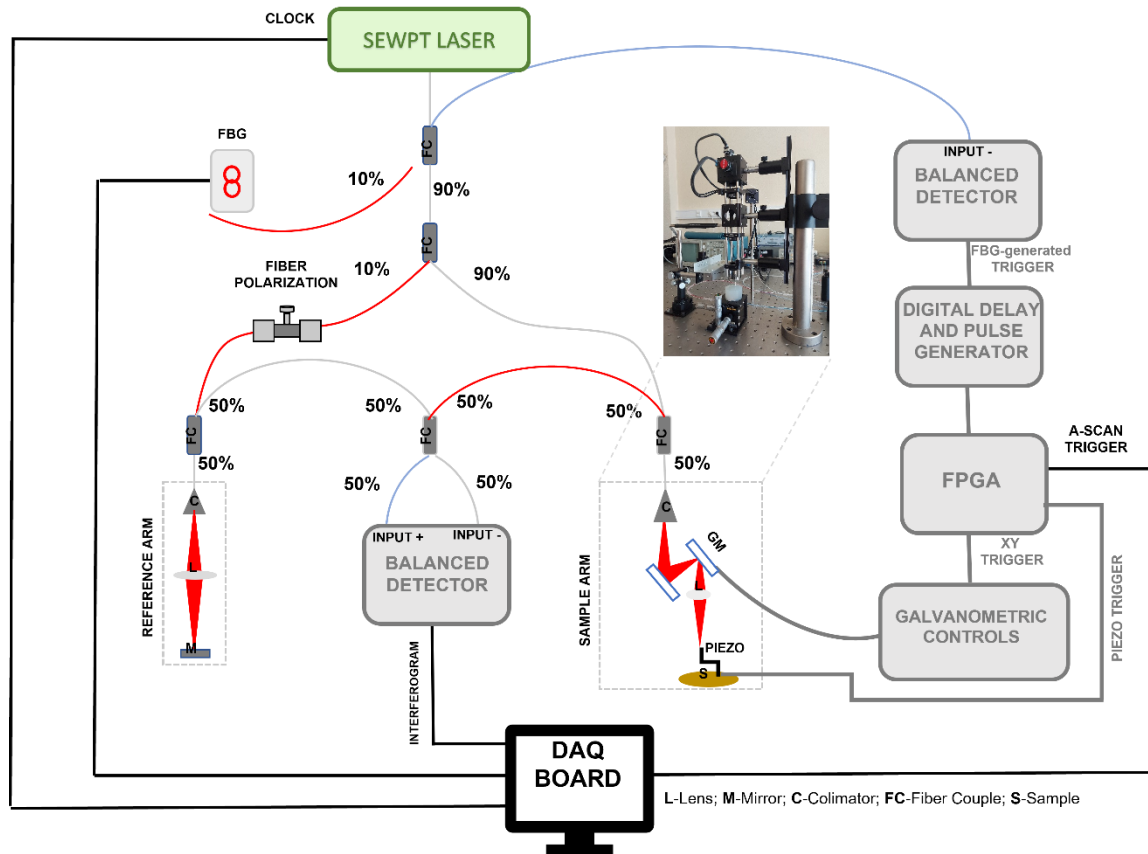
Figure 9 Schematic representation of the SS-OCE system employed.

6.1.1. Laser Source

The laser source used in this study is the OCT Axsun Swept-Source line of lasers from Excelitas, Asslar, Germany. This swept source is the laser Model SSOCT-1060 shown in Figure 10. It powers unmatched tuning bandwidth, output power, scanning speed and coherence length to enable state-of-the-art performance in next generation OCT systems [36].

The laser wavelength centered around 1040 nm with the range of wavelengths between 985 nm and 1095 nm (bandwidth of 100 nm). This range emits with a scan rate of 100 kHz, for OCT imaging [36]. Using a tunable Fabry-Perot filter placed at one end of the laser cavity, it achieves the appropriate wavelengths.

Figure 10 The Laser [36].

6.1.2. System temporal and phase stability.

In OCE systems based on SD-OCT the laser operating principle is static, facilitating the achievement of phase stability. In contrast, the OCE system used in this study is based on a SS-OCT system. The mechanical sweeping movement of the laser causes frequency jitters. It is necessary to ensure synchronisation between data acquisition and laser scanning to improve the phase stability [37].

In phase-resolved measurements, phase stability must be achieved to guarantee measurement precision. In the OCE system used in this study, a MZI clock signal and FBG-generated triggers were used to improve timing synchronization, and therefore, phase stability.

A FBG is a periodic or aperiodic perturbation of the effective refractive index in the core of an optical fibre. Typically, this perturbation is approximately periodic over a given length with a period on the order of hundreds of nanometres, or much longer in case of long fibber gratings [33].

FBGs are made by laterally exposing the core of a single-mode fiber to a periodic pattern of intense laser light. The exposure produces a permanent increase in the refractive index of the fiber's core, creating a fixed index modulation according to the exposure pattern [33].

The K-clock is directly used as the clock for DAQ board. It is uniform in wave space as required for discrete Fourier Transform and provides an additional input on the wavelength scan. This signal controls the acquisition of each sample and gives an indication of the correct times for the acquisition. During the acquisition it oscillates at an average frequency

of 310 MHz, varying ±20% in its frequencies. These oscillations are necessary to linearize the acquisition in k-space since the generated interference signal is not linearly distributed in k-space. After all samples have been acquired, the clock signal clock oscillates more steadily and less frequently, a dummy clock. This clock signal maintains temporal stability by keeping the gap between the end of one acquisition and the start of another filled [37].

To verify the effectiveness of the solutions implemented on temporal, and therefore phase stability, the timing consistency of consecutive interference fringes was measured using a gold-coated mirror as a sample. Timing consistency was given by the standard deviation of the arrival time of consecutive interference fringes at zero-crossing. A cubic interpolation of the data was performed to achieve finer temporal resolution (data point intervals of 3.5 ps) [37].

The Figure 11 quantifies the phase stability. Figure 11 (a) shows the overlapping interference fringes and their temporal displacement. Figure 11 (b) shows the corresponding histograms. The system´s phase stability was checked at the beginning of each experimental session.
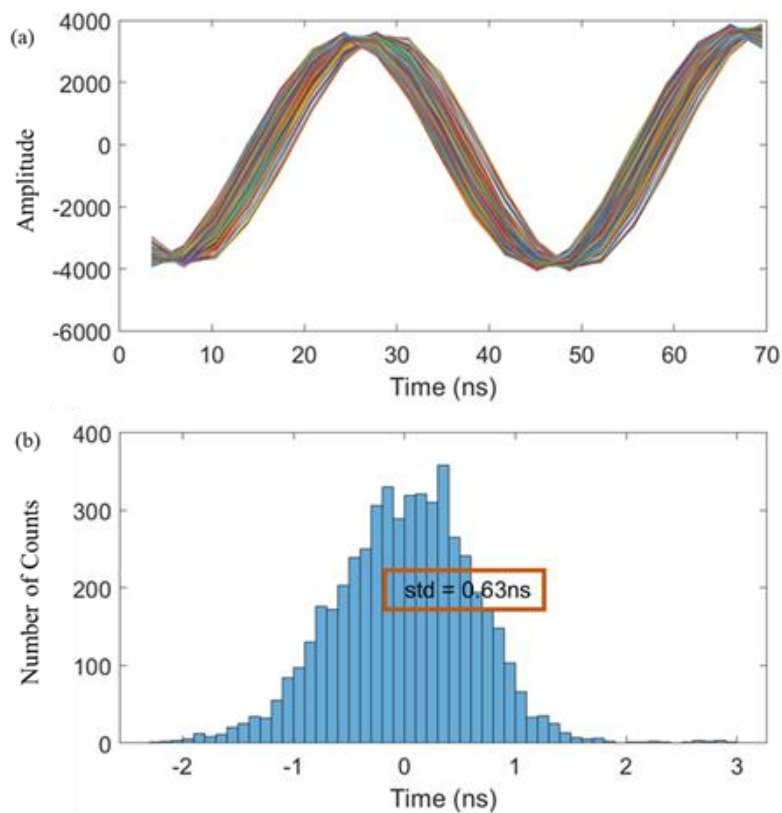

Figure 11 Phase stability quantification: overlay of the interference fringes (a) and timing consisting of zero crossing (b).

6.2.Image acquisition protocols

There are several steps that were followed so that the image acquisition was done correctly. Before the acquisition of any OCE image, it was necessary to check the alignment of the system. For this purpose, a gold-coated mirror was placed underneath the laser beam at the position where the signal intensity of the A-scan allowed to obtain the highest signal-to-noise ratio (SNR). The first acquisition is static OCT structural volume, i.e, without sample motion.

One of the goals of this project was to perform *in vivo* measurements in volunteers. It was necessary to develop an adaptor to allow image acquisitions of the skin *in vivo*. Several features were taken into consideration during development: (1) it should be comfortable for the subject, (2) it must guarantee that the imaged are a remains still during acquisition, and (3) it must be reproducible. The setup configuration for human skin image can be seen in Figure 12. It combines a vacuum pillow combined with a skin-interface adapter, placed at the objectives' focal plane, for arm positioning and stabilization. With this configuration it was possible to position the subjected arm comfortably, while maintaining it at a fixed position, replicable between measurement acquisitions, subjects, and experimental sessions. The piezo lateral position relative to the OCT scanning line was controlled using ruled dovetail optical rail. A piezo-position controller, implemented in the skin-interface adapter, was used to further verify the piezo end-position, and guarantee that the same relative lateral distance was used between experiments.
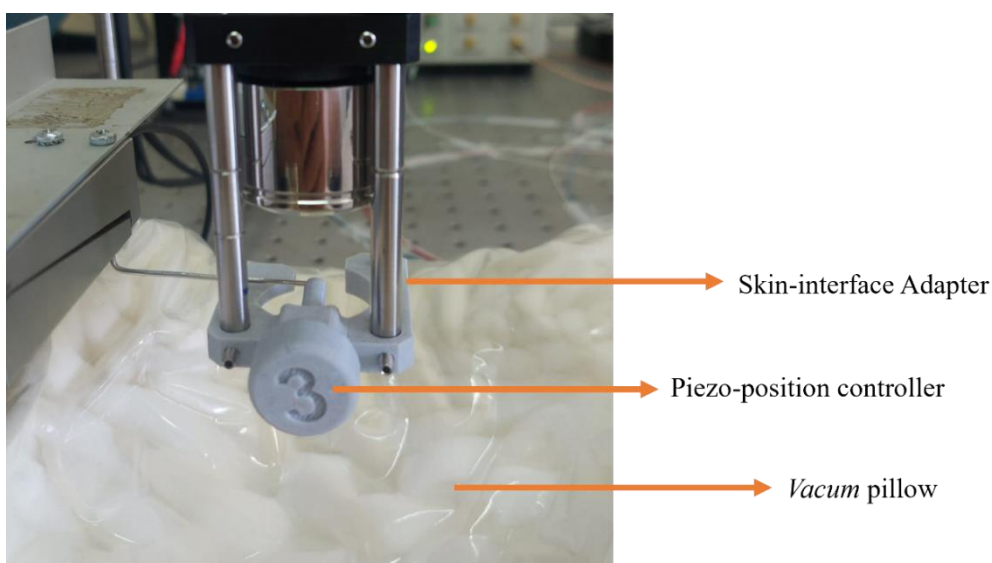

Figure 12 Setup for skin acquisition.

It was also important to ensure that the relative distance between the piezo and the sample was maintained throughout the measurements. For this, we developed a protocol that was reproducible.

1. The gold-coated mirror was placed on to the sample holder and its depth position was checked so that the A-scan signal intensity had the highest possible SNR. In addition, it was ensured that the observed signal did not correspond to the conjugate signal.
2. The mirror position was the used to adjust the relative position the piezo.
3. The mirror was removed from the holder and the sample was placed in the mirror same position, controlled using the OCT interference signal.

OCE data were acquired using M-B acquisition mode. In this acquisition mode, for each laser incidence point on the sample, a number k of elastograms with N points was acquired. Once the acquisition of these elastograms was concluded, the laser was laterally shifted and a new set of k elastograms was acquired. The process was repeated for a set of M points. The result of each acquisition was a MB scan: a volume (x,y,z) of elastograms corresponding to the registration of a B-scan (for a transverse plane to the sample) for T time instants, with a time step of 10 us. For the acquisition of these volumes, a synchronization process between the data acquisition and the signal generator responsible for controlling the mechanical excitation had also been previously implemented. The galvanometer was synchronized with the M trigger and the mechanical excitation. The synchronization scheme is shown in Figure 13.
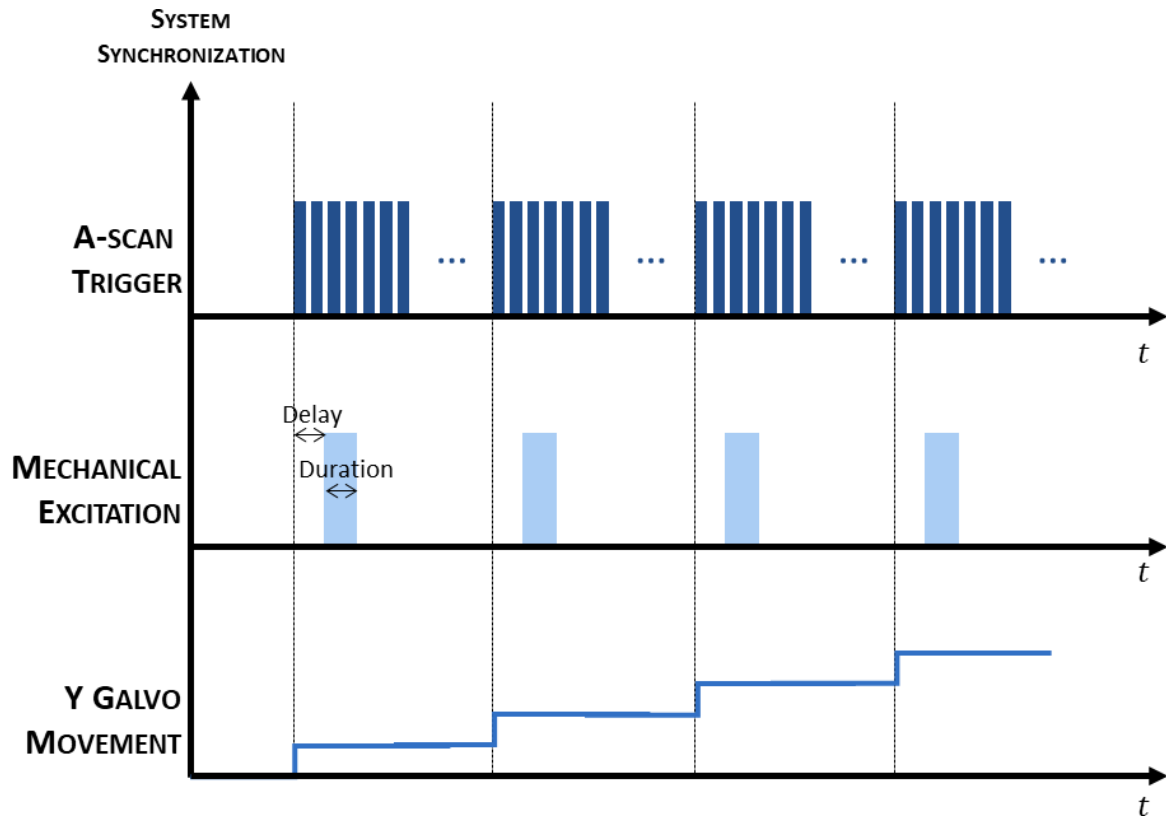
Figure 13 System Sinchronization.

In this study, two scanning configurations were tested to understand the relationship between the mechanical pulse properties and the displacement induced.

In setup 1, shown in Figure 14, the surface motion was induced in the direction of OCT scanning line. The piezo was placed about 3 mm from the OCT scanning line. In setup 2, shown in Figure 15, surface motion was induced perpendicularly to the OCT scanning line direction. The piezo was placed about 1.5 mm from OCT scanning line. The surface motion, in both, setups was induced using transient pulses with fixed amplitude and duration.

In the setup 1 the data were collected using the M-B scanning protocol (512 B-scans x 512 M-scans). The images were taken at 512 lateral positions covering approximately 5 mm, in steps of 9.77 μm. With this setup we were able to observe displacement waves. However, we would need to use complex trigonometry to obtain parameters such as the propagation velocity and hence the Young's modulus. To make it easier to access these parameters we changed the configuration of the system.

The configuration was changed to that shown in Figure 15. A 768x256 MB-scan data acquisition protocol was used. Images were taken at 768 axial positions and a 5 mm line

was imaged in 19.53 μm steps (256 lateral positions). With this setup we observed the wave propagation over time and thus easily access parameters such as wave propagation speed.

For both configurations, surface motion was induced at each lateral location using transient pulses with amplitude of 50 mVpp and a pulse width of 500 μs with a delay of 100 μs.

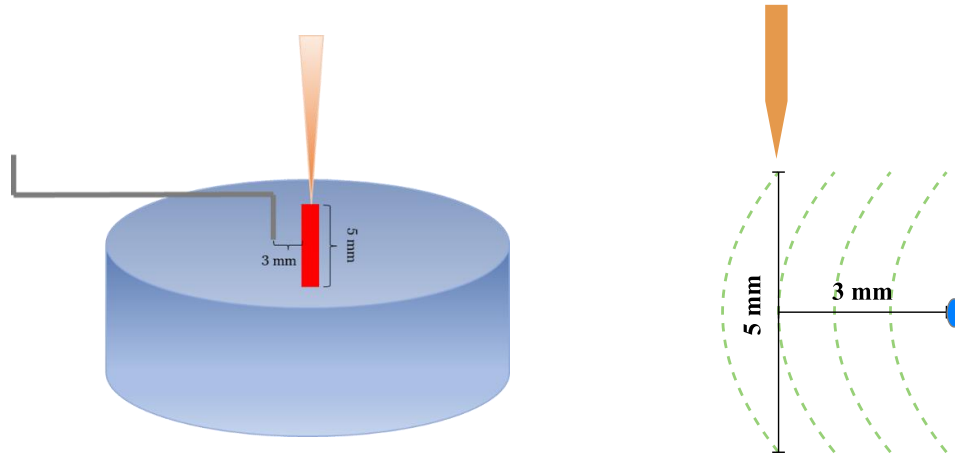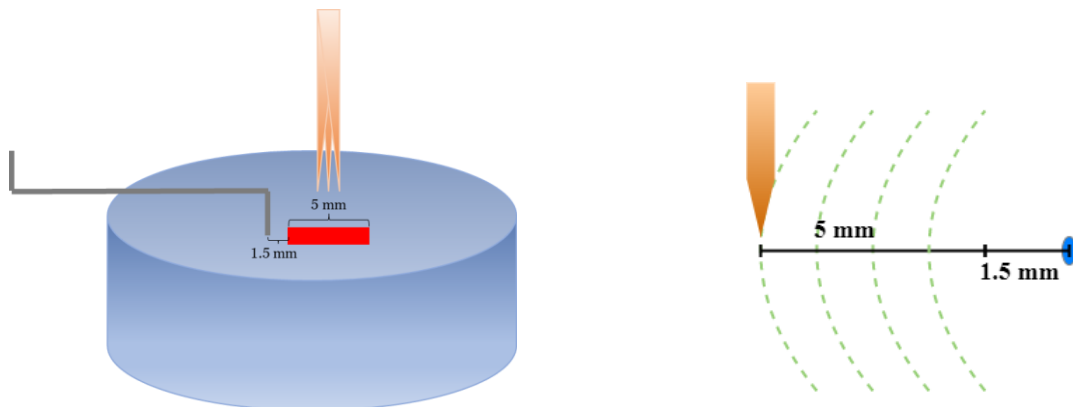Figure 14 Setup 1.

Figure 15 Setup 2.

6.3.   Image analysis

As mentioned in section 3.2.1, the displacement Δd is correlated with the phase difference, $\Delta \varphi$ by the equation (2). The displacement, Δd, depends on the sample's refractive index of the sample, n.

For the skin we found in the literature the value of 1.4 for the refractive index [38]. For phantoms, the refractive index is given by:

$$n = 0.0014x + 1.33 \text{ (3)}$$

where x is the phantom's agarose concentration [39].

From the displacement map we can obtain the velocity value. Figure 16 shows the spatio-temporal propagation of the Rayleigh wave in the sample. The slope m of the line plot represents the wave speed [22]:

$$v = \frac{d}{\Delta t} \; (6)$$

The value of d is a known value that depends on the image size and can be chosen during the acquisition.
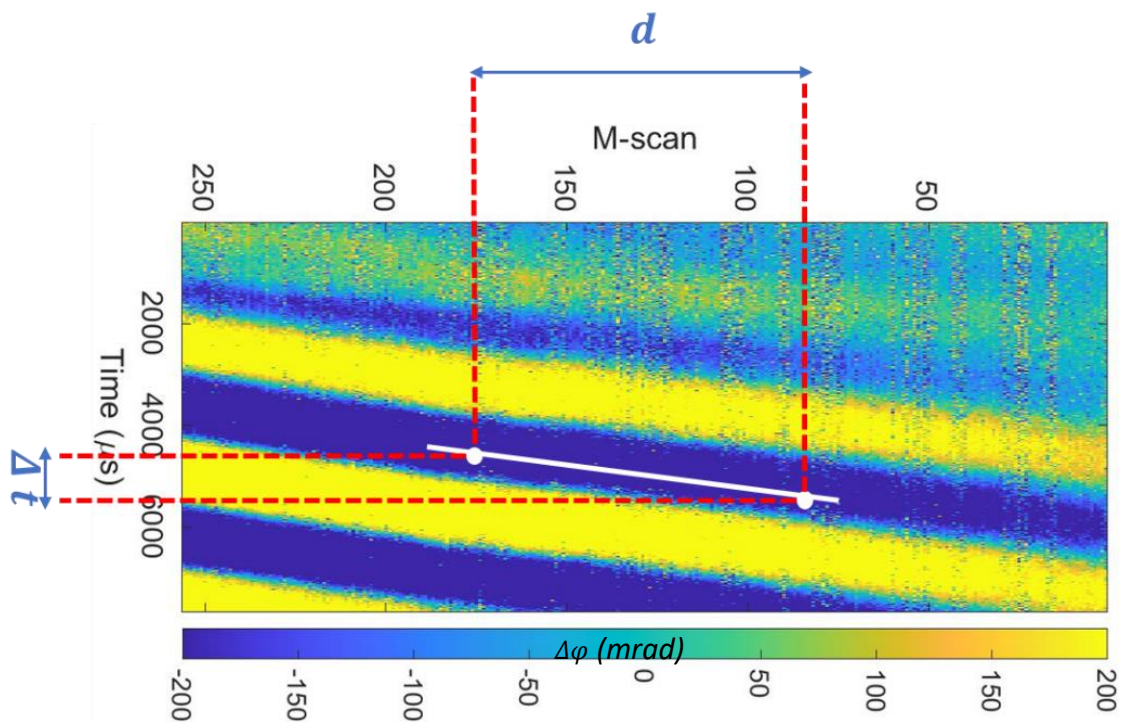

Figure 16 The spatio-temporal propagation of the wave. Colormap represents displacements.

The Rayleigh wave velocity (C_r) relates with the shear wave velocity through the equation:

$$\eta = \frac{C_r}{C_s} \cong 0.955 \; (7)$$

This root shows that, as with shear waves, the velocity of Rayleigh waves only depends on one Lamé parameter (μ). From the Rayleigh wave velocity, it is possible to directly infer the Young's modulus (E):

$$E = 3\mu = 3\rho C_s^{\,2} \approx 3.3 \; \rho C_R^{\,2}$$

6.4. Samples

6.4.1. Phantoms

In the preliminary studies we used phantoms with different agarose concentration that result in different elasticities. This samples are essential to elastic imaging investigations.

These homogeneous agarose phantoms, as the one shown in Figure 17, possess characteristics that mimic tissue. They were prepared by gently mixing, while stirring, agar with distilled water at high temperature (85 $°C$) at concentrations of 10 g/L, 15 g/L, and 25 g/L. To increase optical dispersion glass microspheres were added to the mixture which was then placed in molding containers and cured for 24 h. The phantoms produced were cylindrical with diameters and heights of approximately 5.2 cm and 3.5 cm, respectively.

The phantoms are well preserved in distilled water.

Figure 17 Phantom.

6.4.2. Volunteers skin

In OCE applied to dermatology we performed two tests: (i) evaluate the effect of an anti-aging cream on skin elasticity; (ii) evaluate the difference of skin elasticity of different locations. The number and characteristics of the volunteers are described in the results. All *in vivo* experiments were done on healthy volunteers. The study followed the principles of the World Medical Association's Declaration of Helsinki. Informed consent was obtained from each volunteer.
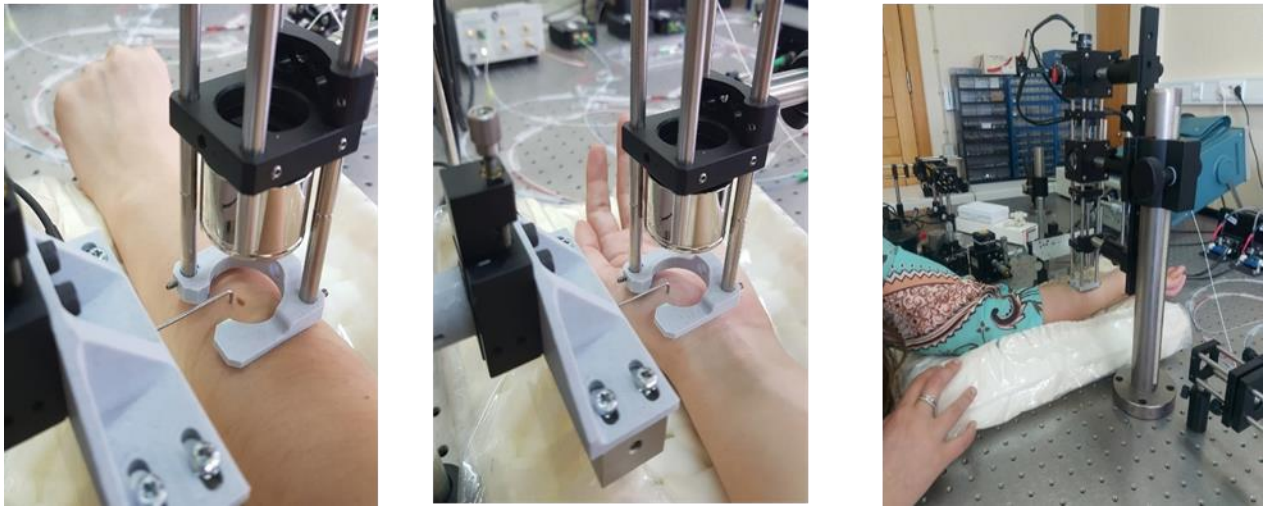
Figure 18 *In vivo* acquisitions.

6.5. Statistical Analysis

In the development of this thesis project, we made *in vivo* acquisitions in human skin from which we obtained a set of data. We analyzed a subset of the population (a sample) that are primary data since they were collected specifically for this study.

Samples are paired since they are constituted using the same experimental subjects, or homologous (e.g., the same variable is measured before and after the application of the cream).

To test the significance of cream application and the factors that are able to influence skin elasticity, comparison of population parameters from the samples is essential. There are basically two methodologies to perform these types of tests: parametric tests and non-parametric tests. Parametric tests require that the shape of the sample distribution is known (being the Normal distribution is the most used) while the non-parametric tests can be applied when the sample distribution is not known the sample distribution (although they have other conditions of application) and should be applied as an alternative to parametric tests.

To know which of the data analysis methodologies to opt for, it is first necessary to test the normality of the distribution. There are many tests for the assessment of normality who compare scores in the sample to a normally distributed set of scores with the same mean

and standard deviation. For these cases, the null hypothesis is that "the sampling distribution is normal". If the test is significant, the distribution is non-normal.

The Kolmogorov-Smirnov (k-S) test is the most used and the one used in this work (using *Matlab*). The K-S test is an empirical distribution function (EDF) in which the theoretical cumulative distribution function of the test distribution is contrasted with the EDF of the data.

$$\begin{cases} H_0: X \sim N(\mu, \sigma) \\ H_1 : X \; not \; normal \; distribution \end{cases}$$

As data from the measurements carried out within the scope of this project failed the normality test it is necessary to apply non-parametric tests. The fact that the sample is quite small (only 3 volunteers) is also a factor for opting for non-parametric tests.

The non-parametric test chosen to analyze the data was the Wilcoxon Signed Rank Test. This test compares two dependent samples with ordinal data. The data were tested using the *signrank* function of *Matlab*:

$$[p, h] = signrank(x, y)$$

This function returns the p-value of a two-sided paired test for the null hypothesis that x - y comes from a distribution with zero median. For p-values less than 0.05 the data was considered statistically relevant.

7. Results

7.1. Agarose Phantoms

As mentioned in section 6.4.1, for these experiments, we used phantoms with different elastic properties. These were achieved by changing the phantom's agarose concentration (10 g/L (ph 1), 15 g/L (ph 2), 25 g/L (ph 3)). The higher the agarose concentration the lower the phantom's elasticity. The phantoms were used to understand the correlation between the displacement curves and the pulses used. The parameters were then optimized for skin acquisitions.

7.1.1. Influence of pulse width and elasticity in displacement induced

Under dynamic conditions, transient pulses induce surface motions in homogeneous agarose phantoms. To test the influence of pulse width on induced displacement, pulse widths of 100 µs, 200 µs, 300 µs, 400 µs and 500 µs were used, with a fixed delay of 200 µs. The piezo actuator was positioned centrally ~3 mm from the OCT beam scanning direction as ilustred in Figure 14 (setup 1).

The induced displacements were measured on the 3 phantoms. For each phantom, acquisitions were performed at 3 non-overlapping positions of interest using the same pulse specifications.

Figure 19 shows the displacement induced over time (at a given axial position) at the phantom surface (ph2) using transient pulses with different widths. Data was filtered using the *Savitzky-Golay* smoothing filter of polynomial order 3 and frame length of approximately 99 µs.
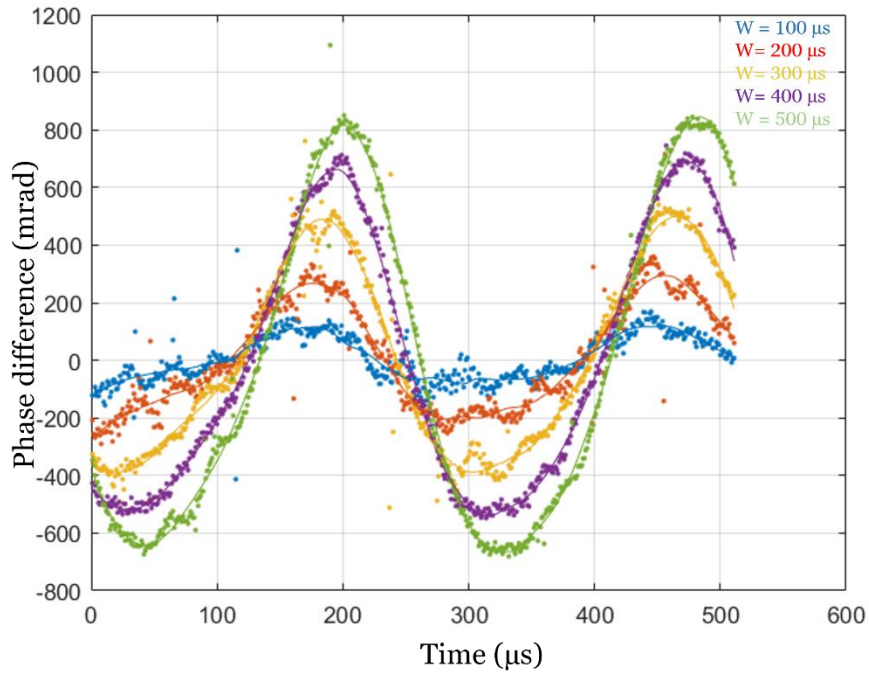
Figure 19 Displacement induced over time for different pulse widths. The dots represent the real data and the continuous line the filtered data.

Figure 20 shows the maximum phase difference as a function of pulse width for the different samples. Data represented as $mean \pm standard\ deviation\ (sd)$. As visible in the graph, depending on the sample elasticity, the same transient pulse will induce different responses. The higher the agarose concentration, the lower the amplitude of the measured phase difference.
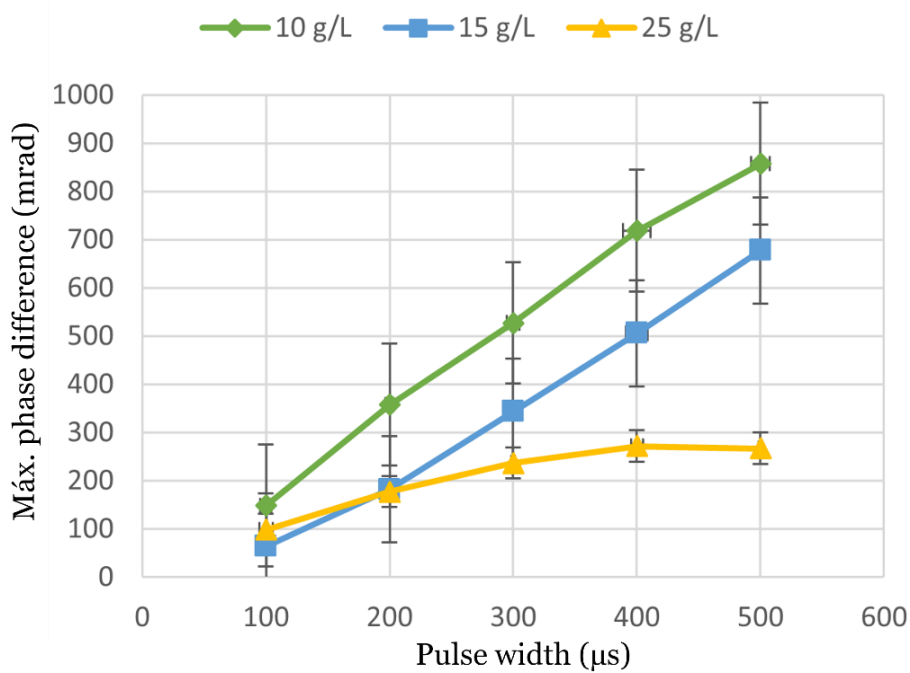

Figure 20 Maximum phase difference value for each pulse width. Data represented as $mean \pm sd.$

To test the influence of elasticity in maximal displacement induced the same transient pulse was applied to three different phantoms. For each phantom acquisitions were performed at 3 positions of interest. In Figure 21 the points correspond to the maximum value of the phase difference obtained for each phantom. Data represented as $mean \pm sd$.

Depending on the sample elasticity, the same transient pulse will induce different responses. As expected, the higher the phantom elasticity, the higher the amplitude of the measured phase difference, and consequently the higher the tissue displacement.
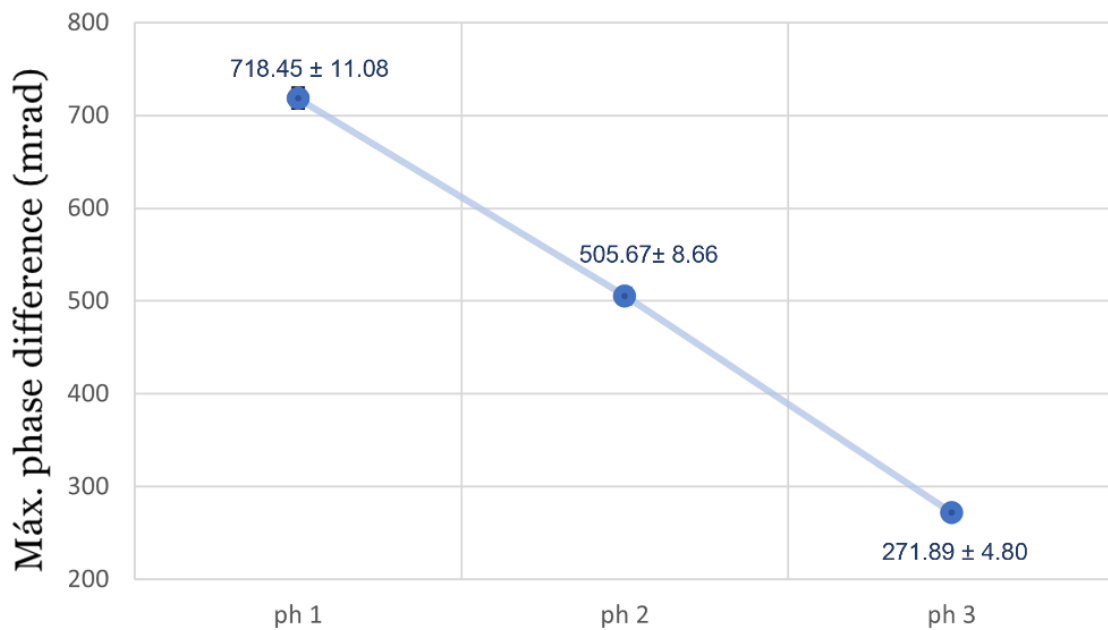

Figure 21 Maximum phase difference value for each phantom. Data represented as $mean \pm sd$.

7.1.2. Influence of elasticity in Rayleigh wave amplitude attenuation

To test the influence of elasticity in Rayleigh wave attenuation, setup 2 was applied. The same transient pulse (*amplitude = 50 mVpp; delay = 100 µs; width = 400 µs*) was applied to three different phantoms. The piezoelectric actuator was positioned laterally at approximately 1.5 *mm* from the OCT beam scanning line as illustrated in Figure 15.

Figure 22 shows an example of the spatiotemporal displacement map for one of the phantoms and the displacement curves at three lateral locations at progressively higher distances from the piezoelectric actuator (0, 2.5, and 5 *mm*).
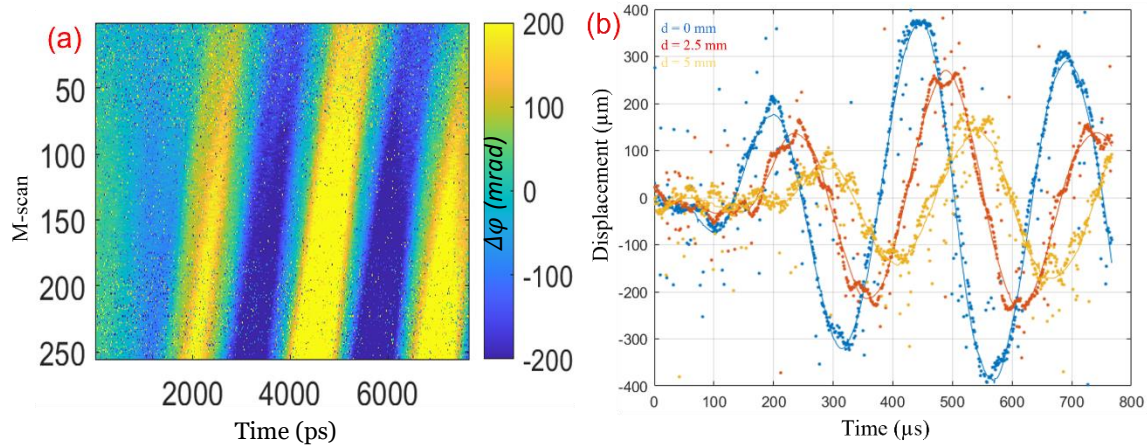

Figure 22 Spatiotemporal displacement map of the phantom surface (A), displacement curves at three lateral locations at progressively higher distances from the piezoelectric actuator (B). The dots represent the real data and the continuous line the filtered data.

Figure 23 shows the motion induced on the surface of the different phantoms over time for a given axial position. It is perceptible the difference in displacement over time for the different phantoms. We observe that for the phantom with higher elasticity (ph1), the maximum value of the phase difference is reached later compared to the phantom with lower elasticity (ph3). In addition, although the pulse delay was kept constant throughout the experiments, the induced displacement was detected consecutively sooner with the increase of phantoms' agarose concentration.
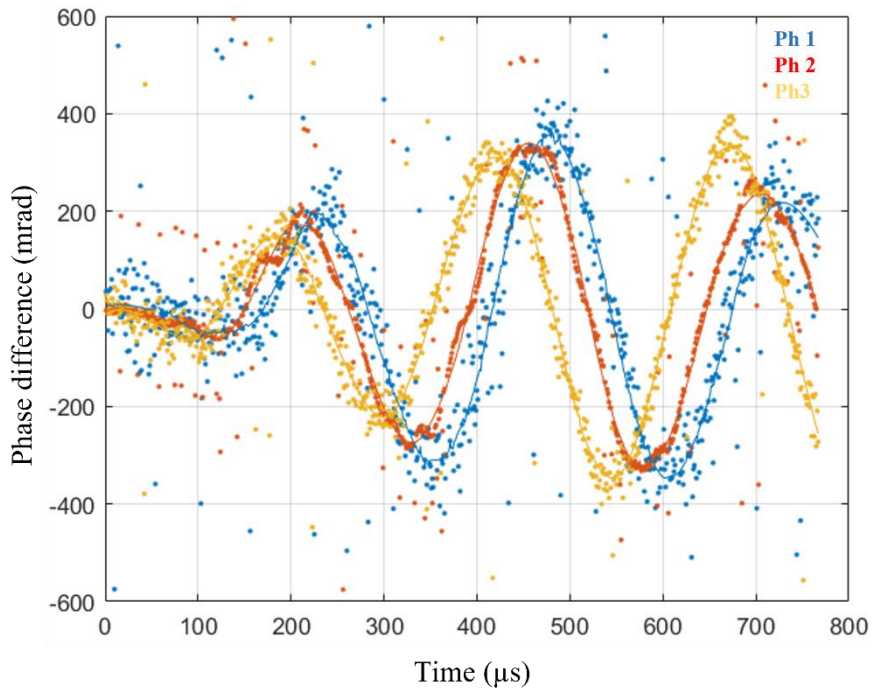
Figure 23 Displacement induced over time for each phantom. The dots represent the real data and the continuous line the filtered data.

Observing the Figure 23 we also realize that the amplitude of the Rayleigh wave is attenuated as it propagates on the surface of the phantoms further away from the excitation point. In the Figure 24 the attenuation of the wave amplitude with increasing distance from the excitation point is shown for the phantoms with different concentrations of agarose. Data represented as $mean \pm sd$. As expected, the amplitude of the wave decreases with increasing distance from the piezo position for all phantoms. In addition, the attenuation with distance appears to be higher for phantoms with lower elasticity. As we can observe, the higher the agarose concentration (less elastic phantom) the greater the slope of the straight line.
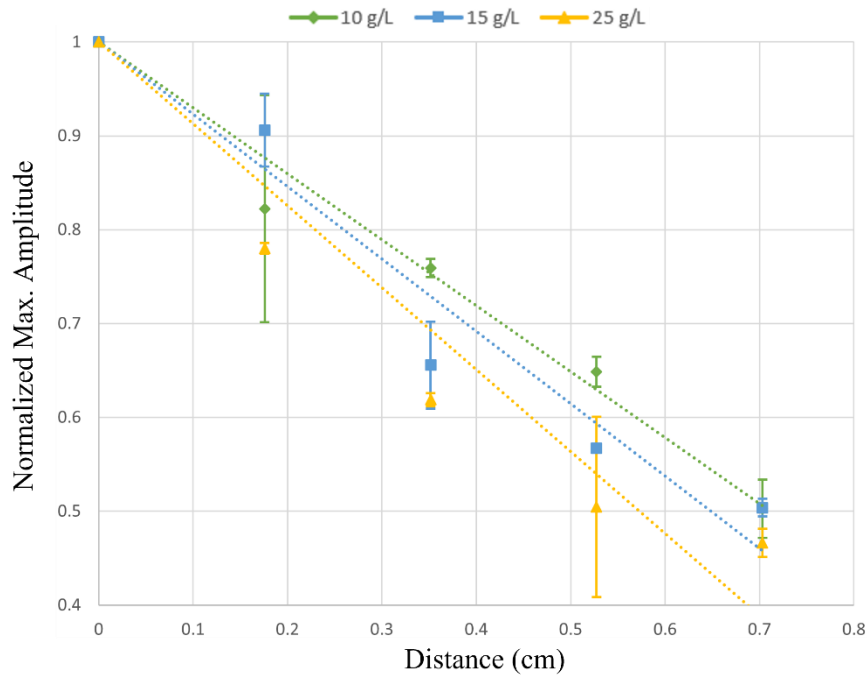
Figure 24 Wave amplitudes recorded at increasing distances from the excitation source. The first point is 1.5 mm from the piezo. Data represented as $mean \pm sd$.

7.1.3. Influence of elasticity in Rayleigh wave propagation speed

The propagation speed of Rayleigh waves at the phantoms surface was estimated from the phase difference between consecutive axial scans, using the kinematic relationship between the propagated distance of a transient pulse Δd during the time Δt ($C_r = \Delta d / \Delta t$). Samples with different elasticities have different Rayleigh wave speeds and consequently different Young´s Modulus.

In Figure 25 the points correspond to the value of the Rayleigh velocity for each phantom and in the Figure 26 points correspond to the value of the Young´s Modulus for each phantom. Data represented as $mean \pm sd$. As expected, the less elastic the phantom (ph 3) the higher the Rayleigh wave speed and consequently higher Young's Modulus.
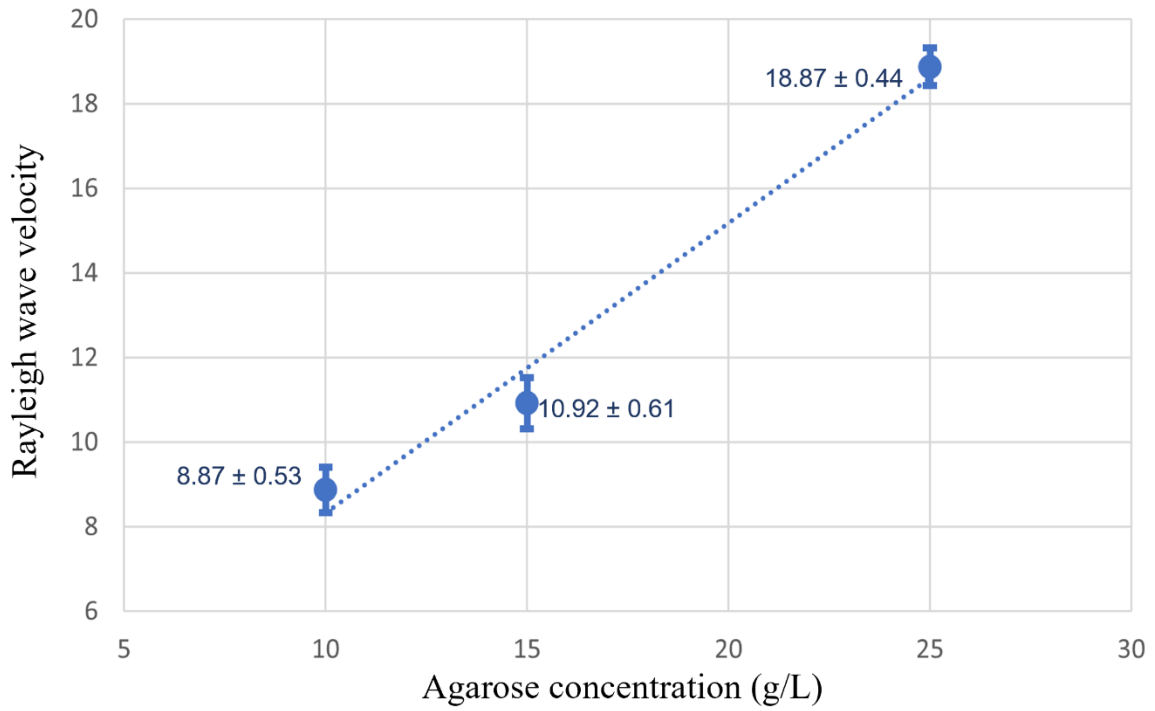
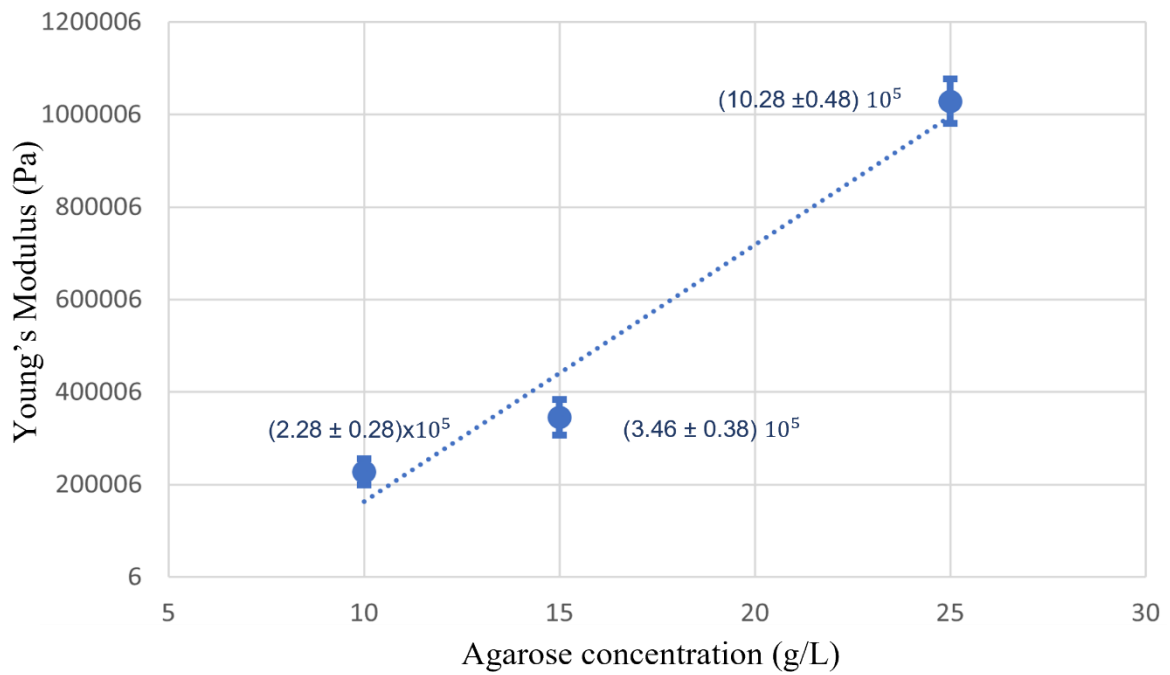Figure 25 Value of Rayleigh wave velocity for each phantom. Data represented as $mean \pm sd$.

Figure 26 Value of Young´s Modulus for each phantom. Data represented as $mean \pm sd$.

7.2. Skin elasticity

Human skin behaves like an elastic tissue: it is possible to measure mechanical properties such as Young's modulus. The more elastic it is, the lower its Young's modulus, as we observed for the tissue-mimicking phantoms. The refractive index of the skin was considered to be 1.4 [38].

7.2.1. Influence of body location and gender

7.2.1.1. Protocol

OCE measurements were initially taken at 9 different locations on the skin of a volunteer. After analyzing the data, three locations of interest were chosen: volar forearm, dorsal forearm and palm. The regions chosen were those where acquisitions were easiest and where results were least discrepant and easier to compare. A structural image for each of these regions was also acquired.

In this proof-of-principle investigation, twelve volunteers were included, six female and six males. In Table 1 is listed the volunteer data (age and gender). For each of the regions, three acquisitions were made. The acquisitions without signal were discarded.

Volunteer	Age (years)	Gender
1	21	Female
2	22	Female
3	23	Female
4	23	Female
5	25	Female
6	35	Female
7	23	Male
8	23	Male
9	25	Male
10	26	Male
11	35	Male
12	60	Male

Table 1 Volunteer's data.

7.2.1.2. Results

Using the system in OCT acquisition mode (without displacement), we collected structural images of the different skin locations. Figure 27 shows examples of the projection for three different areas of the human body: (A) dorsal forearm roughness, (B) volar forearm roughness and (C) palm roughness.
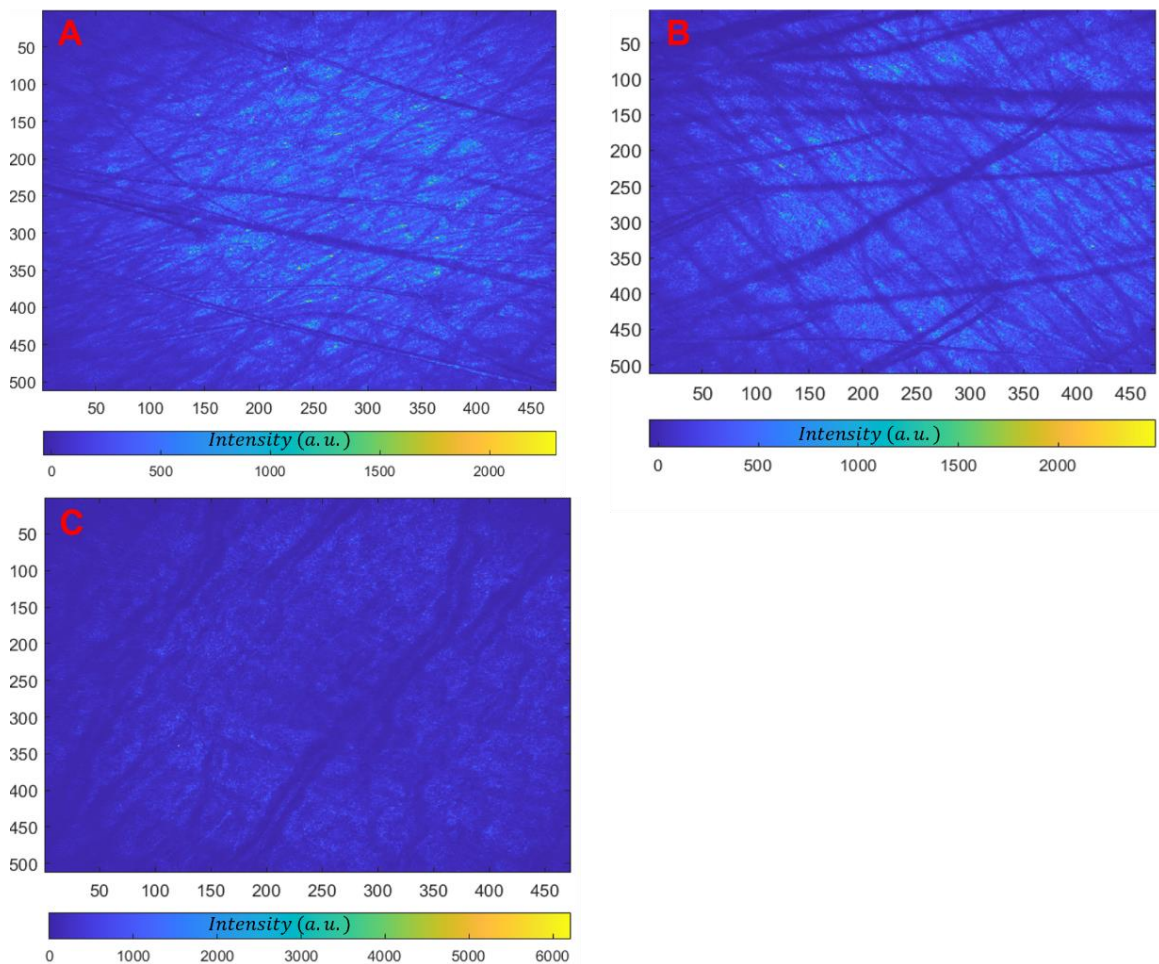

Figure 27 Skin surface projection.

The data collected from the twelve volunteers for the three areas of the human body are shown in Figure 28, Figure 29 and Figure 30. The box plot of Figure 28 shows the variation of Young's modulus in the volunteers for the three parts of the human body. The Young's Modulus values obtained for the area of the volar forearm and dorsal forearm are similar, but for the volar forearm the interquartile range (IQR) is larger, i.e., values are more dispersed. The values obtained for the palm are notably higher than those obtained for the forearm areas. It is also observed that the IQR of the palm data, whereby there is a greater discrepancy in values for the palm acquisitions compared to the forearm acquisitions. The

Young's Modulus values obtained for the palm are statistically different when compared with the volar forearm and dorsal forearm.
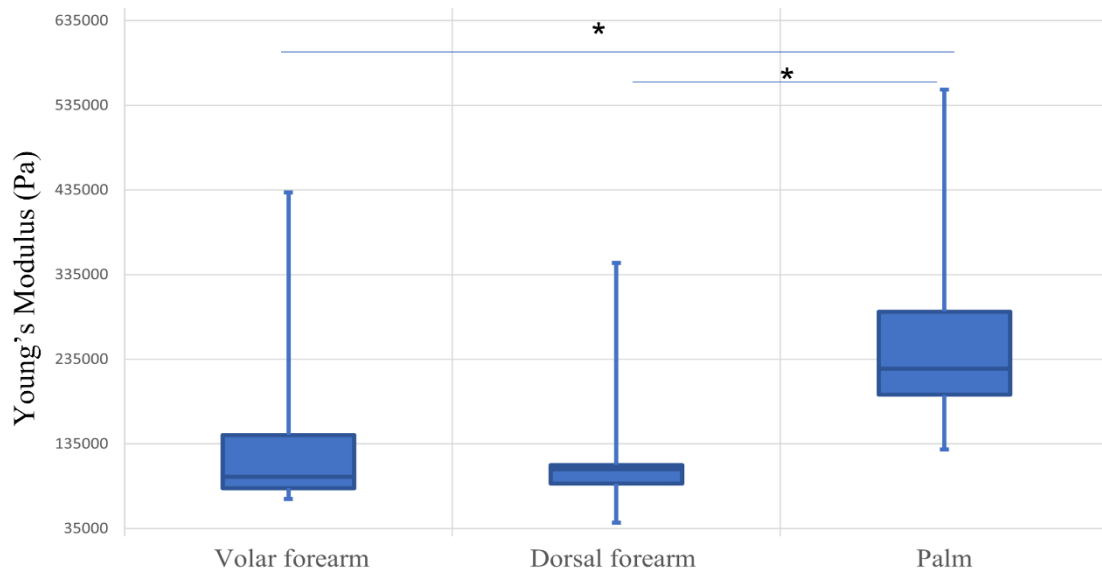
Figure 28 Young´s Modulus obtained for each human body location. *Statistically significant with p < 0.001

The box plot of Figure 29 represents the variation of the data obtained only for female volunteers. The Young's modulus values obtained for the volar forearm area are somewhat lower compared to those obtained for the dorsal forearm, while the values obtained for the palm are notably higher. The results are statistically significant. For these volunteers, the IQR is smaller since the values are less dispersed.
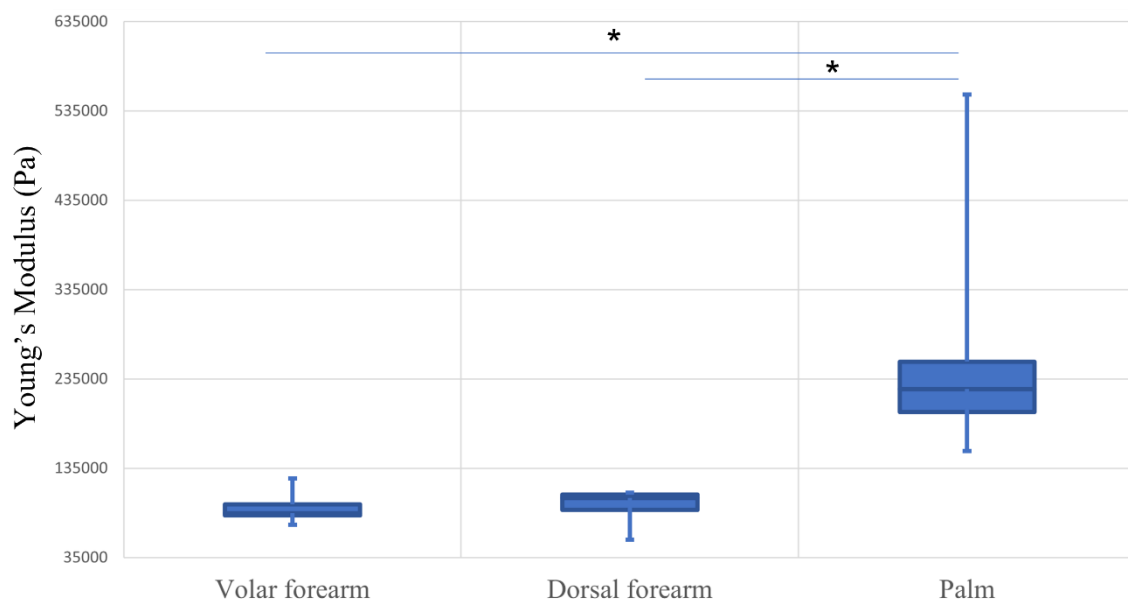

Figure 29 Young´s Modulus obtained for female volunteers. *Statistically significant with p < 0.001

The graph in Figure 30 shows the variation of Young's modulus only for male volunteers for the three sites of interest. The values obtained for the areas of interest follow the pattern of the previous results: upper in the palm and lower in the forearm regions. When compared with the results obtained for female volunteers, we found a greater discrepancy of results (higher IQR). A possible cause is the fact that male volunteers have more heterogeneous characteristics between them. No significant differences were observed in the skin elasticity between the three body regions for male volunteers.
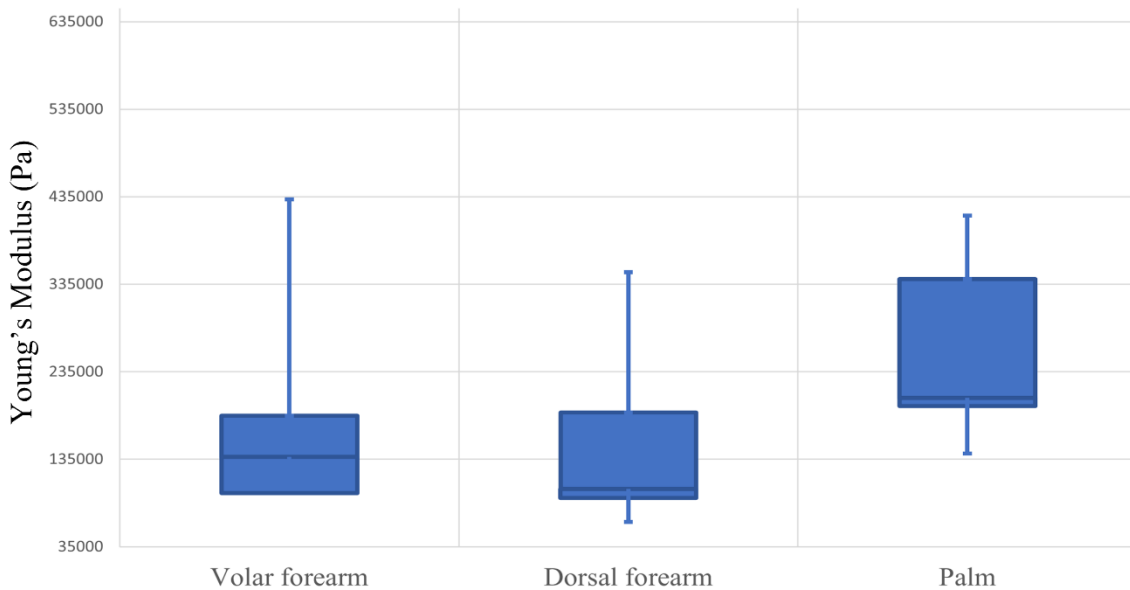
Figure 30 Young´s Modulus obtained for male volunteers.

7.2.2. Anti-aging cream effects

7.2.2.1. Protocol

Three female volunteers, aged between 23 and 35 years old, were included in this proof-of-principle investigation. The volunteers applied daily, for a total of 4 weeks, an anti-aging cream (NIVEA Hyaluron Cellular Filler, Beiersdorf Global AG., Germany) in the left forearm. OCE measurements were performed weekly, starting the day prior to the application of the anti-aging cream. The right forearm was used as a control. No other creams were applied in the control arm. Three regions of interest were acquired in each session.

After interruption of the cream application new OCE measurements were performed for one additional week to evaluate the influence of interrupting anti-aging cream application.

7.2.2.2. Results

Figure 31 show the effect of the anti-ageing cream over the weeks for the set of three volunteers. With the application of anti-aging cream, there is a tendency for a decrease in Young's skin modulus over the weeks following daily application, indicating an increase in skin elasticity. Nonetheless, statistical significance was nor reached. In the week after stopping the cream application (week 5) the Young's modulus increased again. In the control data, the Young's modulus of the tissue fluctuated during the monitoring period.
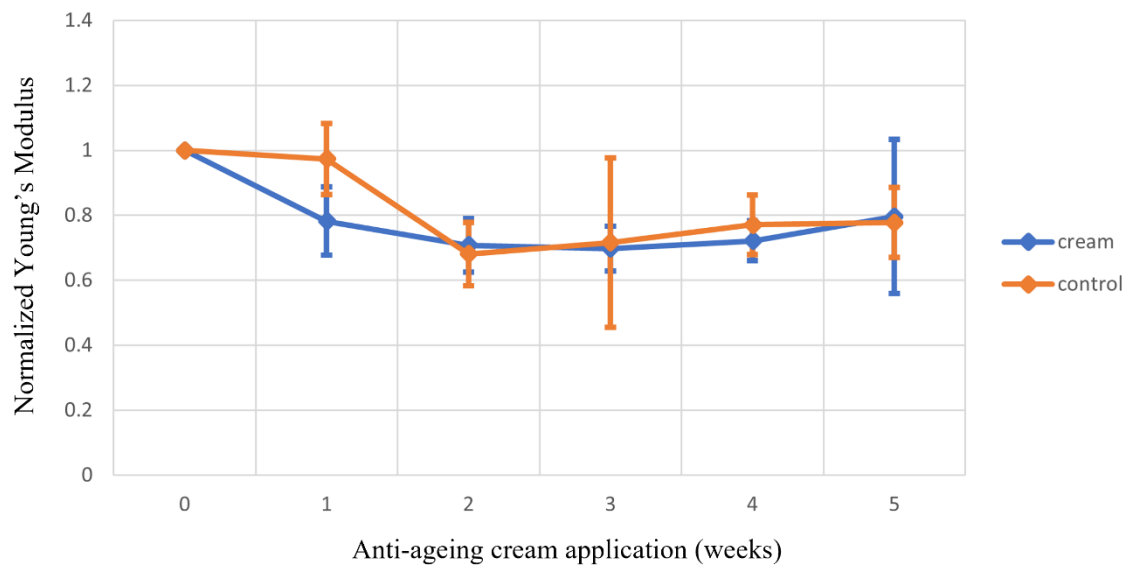
Figure 31 Skin Young's Modulus variation over time with and without anti-aging cream application.

Figure 32 to Figure 34 show the effect of the anti-ageing cream over the weeks for each of the three female volunteers. For the volunteer represented in Figure 32 (female, aged 25) it is found a accentuated decrease in the Young's modulus after application of the cream for one week. In the following weeks the Young's modulus remains practically constant. After the cream is no longer applied, the Young's modulus does not increase again as expected. The control data fluctuate over time.

Figure 32 Skin Young's Modulus variation over time with and without anti-aging cream application, (female, age 25).

For the second volunteer (female, aged 23), the Young's modulus decreases during the three firsts weeks that the cream is applied (Figure 33). In the last week of the cream application the Young's modulus increases unexpectedly. After the interruption of the cream application there is a new increase in Young's modulus to values similar to those obtained in the first acquisition followed by a decrease in the following week. In this case, the values obtained for the control arm follow the same trend as the test arm.
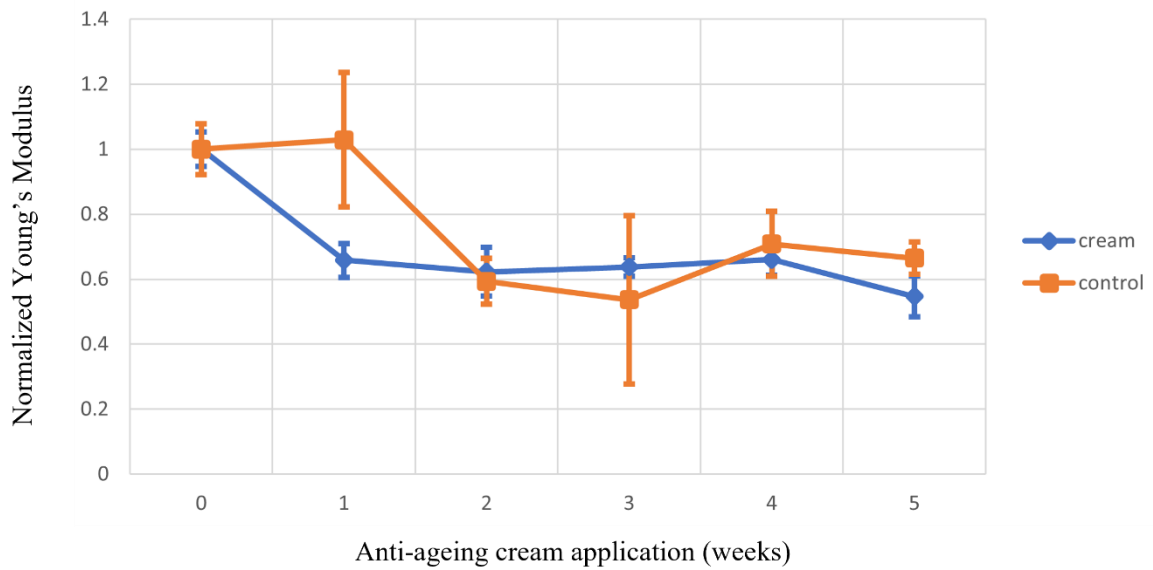

Figure 33 Skin Young's Modulus variation over time with and without anti-aging cream application, (female, age 23).

For the volunteers in Figure 34 (female, aged 35), Young's modulus decreases during the first three weeks that the cream is applied and remains constant the following week. After cream application interruption, the Young's modulus reaches values higher than those recorded in week 0. Control values fluctuate over weeks.
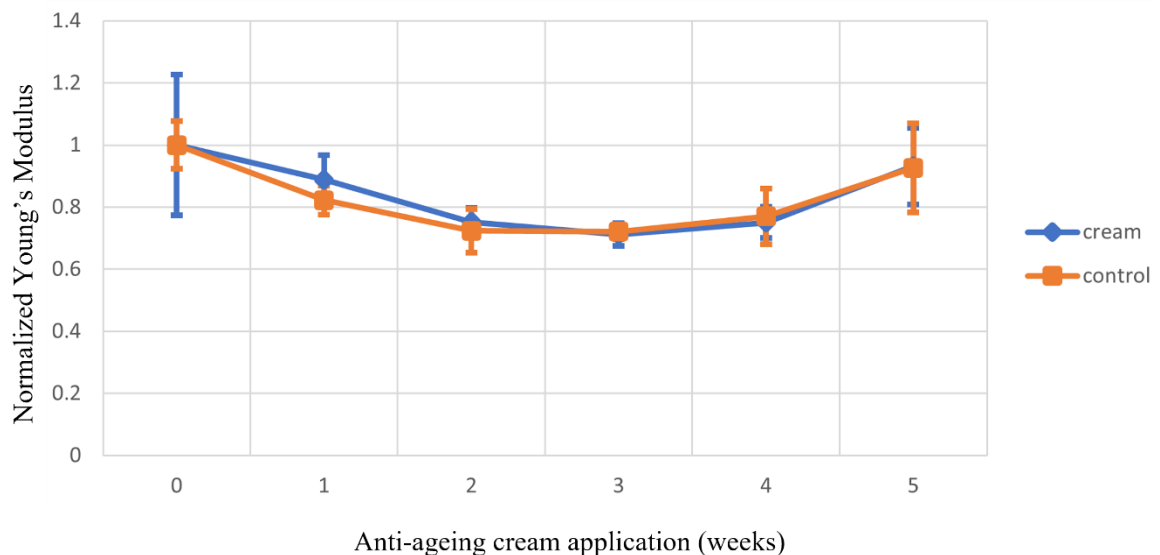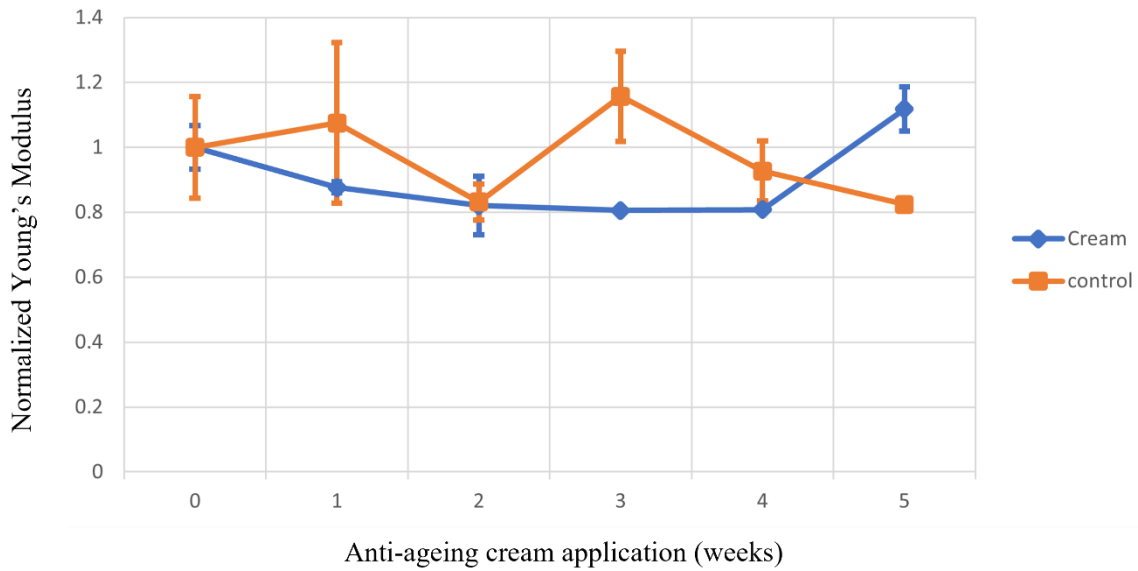

Figure 34 Skin Young's Modulus variation over time with and without anti-aging cream application, (female, age 35).

Young's modulus variations over the study weeks were not statistically relevant for any of the volunteers.

8. Discussion and Conclusions

The primary goals of this work were achieved, both related to the ability of the developed OCE system to distinguish tissues with different elastic properties and the possibility to be used to obtain human skin structural information and to access its elastic properties.

Throughout this study several configurations were tested to optimize the system and obtain as much information about the sample as possible. For this it was necessary to try to understand the ideal settings to make the measurements. Several values were tested for the pulse characteristics: delay, width and amplitude. The sample position was also adjusted throughout the tests to get the best possible results.

In a first approach, the piezoelectric actuator was positioned centrally approximately 3 mm from the scan line of the OCT beam, to induce sample displacement through transient pulses. With this setup it was possible to study the influence of pulse width in displacement induced and the influence of elasticity in maximal displacement induced. As shown in Figure 19, the greater the pulse width the greater the amplitude of the induced displacement in the sample. This was already expected since a larger pulse width will cause a greater vibration and consequently a greater displacement.

In these preliminary experiments, we also showed that the developed OCE system can be used to distinguish tissues with different elastic properties: depending on the sample elasticity, the same transient pulse will induce different responses. The higher the phantom elasticity, the higher the amplitude of the measured phase difference and consequently the higher the tissue displacement as shown in Figure 20 and Figure 21.

In a second approach, the piezo actuator was positioned laterally approximately 1.5 mm from the scan line of the OCT beam. With this setup it was possible to study the influence of elasticity in Rayleigh wave amplitude attenuation and propagation speed. From literature we know that the more elastic a sample is the lower the wave propagation speed and consequently the lower the Young's modulus [40]. In this project we verified this in our samples. As shown in Figure 23, the more elastic phantom reaches the maximal peak amplitude later when compared to the less elastic phantoms.

The results in Figure 24 clearly demonstrate the attenuation of the amplitude wave as it propagates on the surface of each of the phantoms, away from the excitation point. Since

in a more elastic medium the wave propagation speed is lower, the attenuation of the wave propagating in the more elastic phantom will also be lower. Figure 24 corroborates this, since, as already mentioned in section 7.1.2, for the more elastic phantom the slope of the linear fit line is lower than that obtained for the less elastic phantom, which translates into a lower attenuation over time for the more elastic phantom.

As can be seen in Figure 25 and in Figure 26, the less elastic the phantom the higher the corresponding value of Rayleigh's speed and consequently Young's modulus value. These demonstrate that the lower the elasticity, the higher the velocity of propagation and consequently the higher the Young's modulus.

The setup of the second approach was optimized for human skin acquisitions. In this project we evaluated the influence of body location on skin elasticity. Analyzing the graphs in Figure 28 to Figure 30, we can observe that the three chosen body areas have different Young's modulus values, which means that the skin has different elasticities depending on body location.

In all graphs we observe that the palm area has a higher Young's modulus value than the one obtained for the forearm (volar and dorsal). It can be concluded that the skin at the palm of the hand is less elastic than the skin at the forearm. Such a conclusion was to be expected since the skin of the palm has a thick and robust horny layer and has a shortage of natural moisturizing factors. In the graphs we can also observe that the IQR is larger for the palm. This may be due to the fact that the setup was designed to make acquisitions in the forearm, making acquisitions at the palm less consistent.

Applying Wilcox's statistical test, we found that the values obtained for the palm are statistically different from those obtained for the volar forearm and the dorsal forearm for all volunteers as a whole and only for the female volunteers. In the case of the male volunteers, the difference in the values obtained for Young's modulus were not statistically significant. The difference between the values obtained for the volar and dorsal forearm is not statistically relevant for either case. A possible explanation for the fact that the results obtained for the male volunteers were not statistically relevant is the fact that the age range of the volunteers was more disparate when compared to the age range of the female volunteers.

As part of this project, the effect of anti-aging creams on skin elasticity was also studied. Figure 31 shows the changes in Young's modulus over the weeks for the set of three

volunteers. With the application of the cream an initial decrease in the skin Young's Modulus has observed, and it remained low during the treatment time. The values obtained for Young's modulus of the control arm do not follow any trend over time, suffering some fluctuations. The data obtained for each of the volunteers was represented individually to try to understand the fluctuations. The graphs in Figure 32 to Figure 34 show a change in the Young's modulus over the weeks for each volunteer, the difference in the values obtained over the weeks is not statistically relevant for any of the volunteers.

For all these volunteers a decrease in the skin Young's Modulus was observed following anti-aging cream application. This decrease was more pronounced after the first week of application. An increase in the skin Young's Modulus once the application was interrupted was also observed for two of the volunteers. However, all volunteers show large fluctuations in the control arm. In the case of 1 of the volunteers it even follows the same trend as the rest arm. Results may be affected by hormonal changes and external factors such as humidity and room temperature. Nonetheless, our results indicate that these external factors have a higher impact in skin without anti-aging cream application.

8.1. Future work

The first need is to adapt the setup so that the acquisitions are easier to perform and more comfortable for the volunteers and that it allows to make acquisitions in different human body locations.

In the future, the number of subjects in each group will be increased in order to have a larger sample to corroborate the results obtained for skin elasticity in the different locations of the human body. The group of volunteers should also be more homogeneous. The influence of gender and age should also be studied.

In the case of the study of anti-aging creams effects on the skin it is necessary to monitor external factors (such as room temperature and humidity) and possible hormonal changes in the volunteers. Another future work is to analyze the effects of the cream application on the skin structure.

With this work it was possible to obtain, for different locations, the Young's modulus which gives us information about the elasticity of the skin. These studies can predict skin diseases (inflammation, tumours, etc.) and follow-up treatments. Future work could compare the Young's modulus of the skin of a healthy individual with that of an individual with a

dermatological disease. If the difference between the Young's modulus is significant, quantifying the Young's modulus would be a factor to consider when diagnosing certain diseases.

Another area of application to be developed in the future would be the use of OCT images (without elastography) for morphological assessment.

9. References

[1]   K. V. Larin and D. D. Sampson, "Optical coherence elastography – OCT at work in tissue biomechanics [Invited]," *Biomed. Opt. Express*, vol. 8, no. 2, p. 1172, 2017, doi: 10.1364/boe.8.001172.

[2]   J. Fujimoto and E. Swanson, "The development, commercialization, and impact of optical coherence tomography," *Investig. Ophthalmol. Vis. Sci.*, vol. 57, no. 9, pp. OCT1–OCT13, 2016, doi: 10.1167/iovs.16-19963.

[3]   M. L. Gabriele *et al.*, "Optical coherence tomography: History, current status, and laboratory work," *Investig. Ophthalmol. Vis. Sci.*, vol. 52, no. 5, pp. 2425–2436, 2011, doi: 10.1167/iovs.10-6312.

[4]   T. Gambichler, V. Jaedicke, and S. Terras, "Optical coherence tomography in dermatology: Technical and clinical aspects," *Arch. Dermatol. Res.*, vol. 303, no. 7, pp. 457–473, 2011, doi: 10.1007/s00403-011-1152-x.

[5]   A. G. Podoleanu *et al.*, "Optical-coherence tomography, extension to imaging of low coherence interferometry," no. 67851, pp. 67851I-67851I–7, 2007, doi: 10.1117/12.757868.

[6]   K. K. H. Chan, "Spectral Domain Optical Coherence Tomography System Design: Sensitivity Fall-off and Processing Speed Enhancement," *PhD Thesis*, p. 121, 2010.

[7]   F. Prati, M. T. Mallus, F. Imola, and M. Albertucci, "Optical coherence tomography (OCT)," *Catheter. Cardiovasc. Interv. A Knowledge-Based Approach*, vol. 254, no. 5035, pp. 363–375, 2013, doi: 10.1007/978-3-642-27676-7_21.

[8]   D. Huang *et al.*, "Optical coherence tomography.," *Science*, vol. 254, no. 5035, pp. 1178–81, Nov. 1991, doi: 10.1126/science.1957169.

[9]   A. F. Fercher, W. Drexler, C. K. Hitzenberger, and T. Lasser, "Optical coherence tomography - Principles and applications," *Reports Prog. Phys.*, vol. 66, no. 2, pp. 239–303, 2003, doi: 10.1088/0034-4885/66/2/204.

[10]   P. H. Tomlins and R. K. Wang, "Theory, developments and applications of optical coherence tomography," *J. Phys. D. Appl. Phys.*, vol. 38, no. 15, pp. 2519–2535, 2005, doi: 10.1088/0022-3727/38/15/002.

[11] B. J. Vakoc, S. H. Yun, J. F. de Boer, G. J. Tearney, and B. E. Bouma, "Phase-resolved optical frequency domain imaging," *Opt. Express*, vol. 13, no. 14, p. 5483, 2005, doi: 10.1364/opex.13.005483.

[12] V. Jayaraman, J. Jiang, B. Potsaid, G. Cole, J. Fujimoto, and A. Cable, "Design and performance of broadly tunable, narrow line-width, high repetition rate 1310nm VCSELs for swept source optical coherence tomography," *Vertical-Cavity Surface-Emitting Lasers XVI*, vol. 8276, no. April 2015, p. 82760D, 2012, doi: 10.1117/12.906920.

[13] X. Liang, V. Crecea, and S. A. Boppart, "Dynamic optical coherence elastography: A review," *J. Innov. Opt. Health Sci.*, vol. 3, no. 4, pp. 221–233, 2010, doi: 10.1142/S1793545810001180.

[14] J. Ophir, I. Céspedes, H. Ponnekanti, Y. Yazdi, and X. Li, "Elastography: a quantitative method for imaging the elasticity of biological tissues.," *Ultrason. Imaging*, vol. 13, no. 2, pp. 111–34, Apr. 1991, doi: 10.1177/016173469101300201.

[15] B. F. Kennedy, K. M. Kennedy, and D. D. Sampson, "A review of optical coherence elastography: Fundamentals, techniques and prospects," *IEEE J. Sel. Top. Quantum Electron.*, vol. 20, no. 2, pp. 272–288, 2014, doi: 10.1109/JSTQE.2013.2291445.

[16] A. Sarvazyan, T. J. Hall, M. W. Urban, M. Fatemi, S. R. Aglyamov, and B. S. Garra, "An overview of elasticity imaging - an emerging branch of medical imaging.," *Curr. Med. Imaging Rev.*, vol. 7, no. 4, pp. 255–282, 2011, [Online]. Available: http://www.pubmedcentral.nih.gov/articlerender.fcgi?artid=3269947&tool=pmcent rez&rendertype=abstract.

[17] Y. Hong, X. Liu, Z. Li, X. Zhang, M. Chen, and Z. Luo, "Real-time ultrasound elastography in the differential diagnosis of benign and malignant thyroid nodules.," *J. Ultrasound Med.*, vol. 28, no. 7, pp. 861–7, Jul. 2009, doi: 10.7863/jum.2009.28.7.861.

[18] K. D. Costa, "Single-cell elastography: probing for disease with the atomic force microscope.," *Dis. Markers*, vol. 19, no. 2–3, pp. 139–54, doi: 10.1155/2004/482680.

[19] M. Razani, A. Mariampillai, C. Sun, V. X. D. Yang, and M. C. Kolios,

"Biomechanical properties of soft tissue measurement using optical coherence elastography," *Photonic Ther. Diagnostics VIII*, vol. 8207, no. February, p. 820758, 2012, doi: 10.1117/12.920736.

[20] X. Liang and S. A. Boppart, "Dynamic optical coherence elastography and applications," *2009 Asia Commun. Photonics Conf. Exhib. ACP 2009*, no. January 2015, 2009, doi: 10.1117/12.852477.

[21] R. A. Leitgeb, R. M. Werkmeister, C. Blatter, and L. Schmetterer, "Doppler optical coherence tomography.," *Prog. Retin. Eye Res.*, vol. 41, pp. 26–43, Jul. 2014, doi: 10.1016/j.preteyeres.2014.03.004.

[22] F. Zvietcovich and K. V Larin, "Progress in Biomedical Engineering Wave-based optical coherence elastography: The 10-year perspective," 2021, [Online]. Available: https://doi.org/10.1088/2516-1091/ac4512.

[23] R. Adler, "Shear wave elastography in MSK," *Ultrasound Med. Biol.*, vol. 45, no. 8, p. S47, 2019, doi: 10.1016/j.ultrasmedbio.2019.07.565.

[24] *Foundations of Modern Global Seismology*. Elsevier, 2021.

[25] T. Burns, S. Breathnach, N. Cox, and C. Griffiths, Eds., *Rook's Textbook of Dermatology*. Malden, Massachusetts, USA: Blackwell Publishing, Inc., 2004.

[26] S. Del Bino, C. Duval, and F. Bernerd, "Clinical and Biological Characterization of Skin Pigmentation Diversity and Its Consequences on UV Impact," *Int. J. Mol. Sci.*, vol. 19, no. 9, p. 2668, Sep. 2018, doi: 10.3390/ijms19092668.

[27] S. S. Yousef H, Alhajj M, "Anatomy, Skin (Integument), Epidermis," in *Anatomy, Skin (Integument)*, .

[28] K.-M. Lim, "Skin Epidermis and Barrier Function.," *Int. J. Mol. Sci.*, vol. 22, no. 6, Mar. 2021, doi: 10.3390/ijms22063035.

[29] S. Nafisi and H. I. Maibach, "Skin penetration of nanoparticles," in *Emerging Nanotechnologies in Immunology*, Elsevier, 2018, pp. 47–88.

[30] L. M. C. Vasquez-Pinto, E. P. Maldonado, M. P. Raele, M. M. Amaral, and A. Z. de Freitas, "Optical coherence tomography applied to tests of skin care products in humans - a case study," *Ski. Res. Technol.*, vol. 21, no. 1, pp. 90–93, 2015, doi:

10.1111/srt.12161.

[31]   Y. Du *et al.*, "Rapid, noninvasive quantitation of skin disease in systemic sclerosis using optical coherence elastography," *J. Biomed. Opt.*, vol. 21, no. 04, p. 1, 2016, doi: 10.1117/1.jbo.21.4.046002.

[32]   X. Liang and S. A. Boppart, "Biomechanical properties of in vivo human skin from dynamic optical coherence elastography," *IEEE Trans. Biomed. Eng.*, vol. 57, no. 4, pp. 953–959, 2010, doi: 10.1109/TBME.2009.2033464.

[33]   K. O. Hill and G. Meltz, "Fiber Bragg grating technology fundamentals and overview," *J. Light. Technol.*, vol. 15, no. 8, pp. 1263–1276, 1997, doi: 10.1109/50.618320.

[34]   K. Kitayama, Y. Kimura, and S. Seikai, "Fiber-optic logic gate," *Appl. Phys. Lett.*, vol. 46, no. 4, pp. 317–319, Feb. 1985, doi: 10.1063/1.95615.

[35]   Thorlabs, "Balanced Amplified Photodetector," *Thorlabs*, vol. 100, no. January, pp. 1–40, 2019.

[36]   Axsun, "High Speed Swept Laser Engines at 1060 , 1310 , & 1220 nm High Speed Swept Laser Engines at 1060 , 1310 , & 1220 nm Typical Optical Spectra of Axsun Lasers," no. 2, pp. 2–3, 2021.

[37]   Y. Li, S. Moon, J. J. Chen, Z. Zhu, and Z. Chen, "Ultrahigh-sensitive optical coherence elastography," *Light Sci. Appl.*, vol. 9, no. 1, 2020, doi: 10.1038/s41377-020-0297-9.

[38]   A. Bhandari, B. Hamre, Ø. Frette, K. Stamnes, and J. J. Stamnes, "Modeling optical properties of human skin using Mie theory for particles with different size distributions and refractive indices," *Opt. Express*, vol. 19, no. 15, p. 14549, 2011, doi: 10.1364/oe.19.014549.

[39]   E. Fujiwara, T. D. Cabral, M. Sato, H. Oku, and C. M. B. Cordeiro, "Agarose-based structured optical fibre," *Sci. Rep.*, vol. 10, no. 1, pp. 1–8, 2020, doi: 10.1038/s41598-020-64103-3.

[40]   A. Parmar, G. Sharma, S. Sharma, and K. Singh, "Portable Optical Coherence Elastography System with Flexible and Phase Stable Common Path Optical Fiber Probe," *IEEE Access*, vol. 9, pp. 56041–56048, 2021, doi: 10.1109/ACCESS.2021.3071793.